Check for updates

19449194, 2022, 10, Downloaded from https://agupubs.onlinelibrary.wiley.com/doi/10.1029/2022TC007300 by Test, Wiley Online Library on [10/01/2023]. See the Terms and Conditions (https://onlinelibrary.wiley.com/terms-and-conditions) on Wiley Online Library for rules of use; OA articles are governed by the applicable Creative Commons License

Tectonics®

RESEARCH ARTICLE
10.1029/2022TC007300

**Key Points:**

- We present evidence for a large paleo-earthquake on a major intracontinental strike-slip fault from analysis of high-resolution imagery
- The Dzhungarian and Lepsy Faults might have ruptured together in a single event (up to $M_w$ 8.4) with fault slip of up to ~20 m at one site
- A compilation of intracontinental earthquakes shows these faults follow the global earthquake scaling relationships of slip and length

**Supporting Information:**

Supporting Information may be found in the online version of this article.

**Correspondence to:**

C.-H. Tsai,
chia-hsin.tsai@earth.ox.ac.uk

**Citation:**

Tsai, C.-H., Abdrakhmatov, K., Mukambayev, A., Elliott, A. J., Elliott, J. R., Grützner, C., et al. (2022). Probing the upper end of intracontinental earthquake magnitude: A prehistoric example from the Dzhungarian and Lepsy Faults of Kazakhstan. *Tectonics*, *41*, e2022TC007300. https://doi.org/10.1029/2022TC007300

Received 27 MAR 2022
Accepted 19 JUL 2022

**Author Contributions:**

**Conceptualization:** C.-H. Tsai
**Investigation:** C.-H. Tsai, A. J. Elliott, C. Grützner, R. T. Walker, R. Wilkinson
**Methodology:** C.-H. Tsai, J. R. Elliott, E. J. Rhodes, A. H. Ivester
**Supervision:** R. T. Walker
**Writing – original draft:** C.-H. Tsai, R. T. Walker
**Writing – review & editing:** R. T. Walker

© Wiley Periodicals LLC. The Authors. This is an open access article under the terms of the Creative Commons Attribution License, which permits use, distribution and reproduction in any medium, provided the original work is properly cited.

# Probing the Upper End of Intracontinental Earthquake Magnitude: A Prehistoric Example From the Dzhungarian and Lepsy Faults of Kazakhstan

**C.-H. Tsai[1], K. Abdrakhmatov[2], A. Mukambayev[3], A. J. Elliott[4], J. R. Elliott[5], C. Grützner[6], E. J. Rhodes[7], A. H. Ivester[7], R. T. Walker[1], and R. Wilkinson[1]**

[1]COMET, Department of Earth Sciences, University of Oxford, Oxford, UK, [2]Kyrgyz Institute of Seismology, Bishkek, Kyrgyzstan, [3]Kazakhstan National Data Center, Satbayev University, Almaty, Kazakhstan, [4]U.S. Geological Survey, Earthquake Science Center, Moffett Field, CA, USA, [5]COMET, School of Earth and Environment, University of Leeds, Leeds, UK, [6]Institute of Geological Sciences, Friedrich Schiller University Jena, Jena, Germany, [7]Department of Geography, University of Sheffield, Sheffield, UK

**Abstract** The study of surface ruptures is key to understanding the earthquake occurrence of faults especially in the absence of historical events. We present a detailed analysis of geomorphic displacements along the Dzhungarian Fault, which straddles the border of China and Kazakhstan. We use digital elevation models derived from structure-from-motion analysis of Pléiades satellite imagery and drone imagery from specific field sites to measure surface offsets. We provide direct age constraints from alluvial terraces displaced by faulting and indirect dating from morphological analysis of the scarps. We find that the southern 250 km of the fault likely ruptured in a single event in the last 4,000 years, with displacements of 10–15 m, and potentially up to 20 m at one site. We infer that this Dzhungarian rupture is likely linked with a previously identified paleo-earthquake rupture on the Lepsy Fault through a system of splays in the intervening highlands. Though there are remaining uncertainties regarding consistency in age constraints between the two fault ruptures, most of the sites along the two faults are consistent with a most recent event 2,000–4,000 years ago. Rupture on the Dzhungarian Fault alone is likely to have exceeded $M_w$ 8, and the combined Lepsy-Dzhungarian rupture scenario may have been up to $M_w$ 8.4. Despite being at the upper end of known or inferred continental earthquake magnitudes, our proposed scenario combining the 375 km of the Dzhungarian and Lepsy ruptures yields a slip-to-length ratio consistent with global averages and so do other historical intracontinental earthquakes in Central Asia.

**Plain Language Summary** Numerous large, destructive earthquakes have occurred on faults inside the continents in recent centuries. However, comparing to plate-boundary faults, the behaviors of intracontinental faults are not well understood. We undertake a detailed survey of the surface ruptures along the Dzhungarian Fault, one of the major faults in Central Asia. We map and analyze high-resolution satellite and drone imagery. We identify fresh surface ruptures distributed along the southern 250 km of the Dzhungarian Fault. We suggest that these ruptures were produced in a single event which probably caused displacements of up to ~20 m and no <6 m. We also present evidence that the Dzhungarian Fault and its neighboring Lepsy Fault may have ruptured together. Using their combined length, we calculate a slip-to-length ratio which lies within the expected range instead of an unusually high ratio mentioned previously. Our age constraints indicate the most recent event for the two fault ruptures occurred 2,000–4,000 years ago. We estimate the potential maximum earthquake magnitudes to be $M_w$ 8.2 for the Dzhungarian Fault rupturing alone and $M_w$ 8.4 for the combined rupture of the Lepsy-Dzhungarian Faults. This second scenario would be one of the largest magnitudes ever inferred for a continental earthquake.

## 1. Introduction

There is a growing realization that active faults deep within the continental interiors behave in ways that are unexpected given the present understanding of global earthquakes and fault rupture (Bilham & England, 2001; Campbell et al., 2015; Copley et al., 2011; Leonard, 2010; Schmidt & Bürgmann, 2006; Walker et al., 2017; Wells & Coppersmith, 1994). Observation of destructive earthquakes in such regions from historical to recent times show some evidence of spatial and temporal clustering, presenting challenges in the application of standard

19449194, 2022, 10, Downloaded from https://agupubs.onlinelibrary.wiley.com/doi/10.1029/2022TC007300 by Test, Wiley Online Library on [10/01/2023]. See the Terms and Conditions (https://onlinelibrary.wiley.com/terms-and-conditions) on Wiley Online Library for rules of use; OA articles are governed by the applicable Creative Commons License

time-independent models of earthquake occurrence (Liu & Stein, 2016; Salditch et al., 2020; Shimazaki & Nakata, 1980; Sieh, 1996; Stein et al., 2009). Earthquake ruptures in continental interiors can be complex, and there are several examples that show the potential for very large earthquakes to occur on a network of multiple short faults, which may be of particular importance for rupture within diffuse networks of critically stressed faults, as commonly observed in plate-interior settings (Abdrakhmatov et al., 2016; Ainscoe et al., 2019; King et al., 2019; Ross et al., 2019). More fundamentally, there is uncertainty in (a) the degree to which the recent and historical records of earthquakes encompass the maximum likely magnitude of future events (Hu et al., 2021; Pierce et al., 2021; Walker et al., 2021), and (b) the relationships between rupture length, average and maximum surface slip, and magnitude (Leonard, 2010; Manighetti et al., 2007; Ou et al., 2020; Thingbaijam et al., 2017; Wesnousky, 2008).

Some faults in continental interiors rupture in earthquakes with total fault slip significantly larger than expected for their length, according to common slip-to-length ratio estimated as $10^{-4}$–$10^{-5}$ (Leonard, 2010; Scholz, 1982, 1986; Wells & Coppersmith, 1994). For example, the 2001 $M_w$ 7.6 Bhuj earthquake in India involved ∼10 m of slip on a fault extending for 20–30 km laterally, and 20 km in depth (Copley et al., 2011; Schmidt & Bürgmann, 2006), and the 1897 $M_w$ 8.1 earthquake in Assam, India, involved slip of 11–25 m on a 110-km-long fault (Bilham & England, 2001). The occurrence of unusually large amounts of slip may be related to the structural maturity of the faults since it has been proposed that more immature faults tend to fail in more energetic ruptures (e.g., Manighetti et al., 2007). The large seismogenic thicknesses encountered in some intraplate regions are also likely to affect the measured slip, due to larger fault plane area for a given fault length (Jackson et al., 2021; Lu et al., 2018; Stockmeyer et al., 2014). The classification, modeling, and eventual understanding of earthquake occurrence in continental interiors has direct impacts on modern approaches to seismic hazard assessment (Li et al., 2009; Liu & Stein, 2016). However, there are a limited number of examples of earthquakes that demonstrate particular behaviors, or that are studied in sufficient detail to help refine scaling relationships for continental interiors. It is therefore important to re-examine the historical record, and to explore the paleoseismic record to provide databases of sufficiently long duration (e.g., Abdrakhmatov et al., 2016; Baize et al., 2019; Bi et al., 2020; Hu et al., 2021; McCalpin & Carver, 2009; Pantosti et al., 1993; Rizza et al., 2015; Sieh, 1978; Walker et al., 2017; Wallace, 1970; Zhang et al., 2005).

The Tien Shan region of Central Asia is important as a natural laboratory for examining plate-interior earthquake occurrence, with a pristine natural landscape across much of the region providing potential to record discrete earthquake ruptures which occurred in the past several thousands of years (e.g., Avouac et al., 1993; Campbell et al., 2019; Grützner et al., 2017a, 2017b; Rizza et al., 2019; Thompson et al., 2002; Wu et al., 2020). There is also an historical and early instrumental record of very large, apparently clustered, and sometimes complex earthquake ruptures (Abdrakhmatov et al., 1996, 2002; Kalmeteva et al., 2009; Thompson, 2001). The northern Tien Shan region, in particular, experienced a series of large earthquakes ($M$ 6.9–8.3) comprising the 1885 Belovod, 1887 Verny, 1889 Chilik, 1911 Chon-Kemin, and 1938 Chu earthquakes (Arrowsmith et al., 2017; Bogdanovich et al., 1914; Hay, 1888; Krüger et al., 2017; Molnar & Ghose, 2000; Mushketov, 1890; Vilgelmzon, 1947). The 1889 Chilik earthquake is the largest of this apparent sequence, with a moment-magnitude estimated at 8.0–8.3 (Krüger et al., 2017), and apparent rupture on three discrete faults, including both left and right-lateral slip, and with slip of up to 10 m on the central 35-km-long section. The ∼175 km of surface ruptures identified from satellite imagery and field surveys is shorter than expected for the estimated instrumental magnitude relative to global compilations (Abdrakhmatov et al., 2016). The broad distribution of the isoseismals suggests a deep focus of up to ∼40 km (Bindi et al., 2014). Earthquake centroid depths of up to 40 km are determined for some recent earthquakes in the foreland of the main Tien Shan (Chen & Molnar, 1983; Sloan et al., 2011), and it is possible that equivalent rupture depths are possible in the northernmost parts of the Tien Shan itself, though modern-day seismicity in the mountain interior is typically in the range 15–30 km (Figure 1a; Alinaghi & Krüger, 2014; Sloan et al., 2011).

The remarkable size and complexity of the 1889 Chilik earthquake, and of the other earthquakes within the northern Tien Shan sequence (e.g., Abdrakhmatov et al., 2016; Arrowsmith et al., 2017), prompt an investigation of the longer-term behavior of faults in the Tien Shan foreland region. Such studies are required to shed light on the occurrence of large intraplate earthquakes in general, and to better understand the seismic risks posed to the fast growing cities along the northern Tien Shan margin, which would be susceptible to shaking from large earthquakes at the margin and in the foreland (e.g., Amey et al., 2021; Mosca et al., 2019). Few pre-19th century

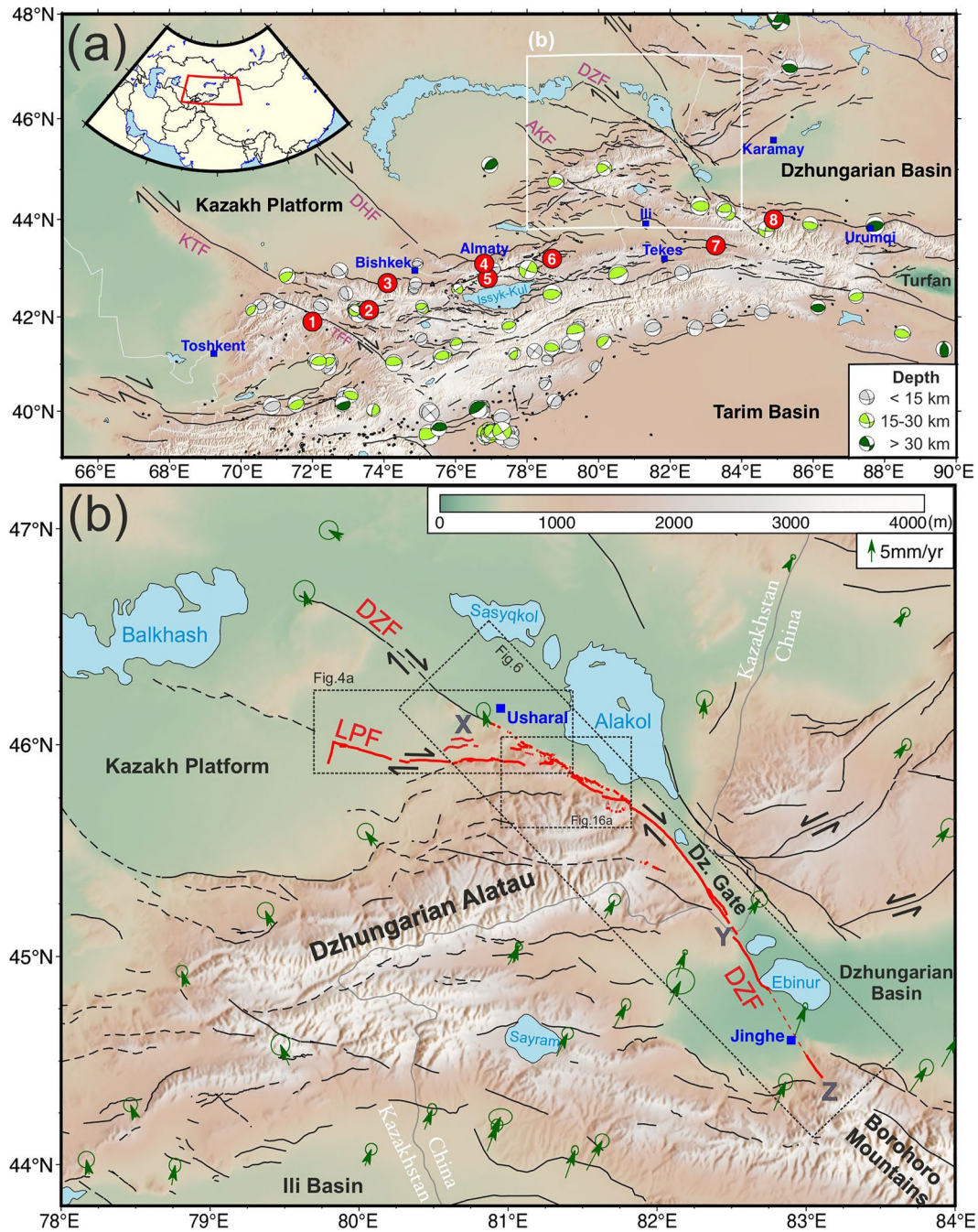


**Figure 1.** (a) Topography, active faults, and selected historical earthquakes in the Tien Shan. Earthquake centroid depths and fault plane solutions are constrained by body wave inversion ($M_w > 5$) from Sloan et al. (2011) and references therein. Black dots are $M_w > 4$ events from 1965 to 2019 from the Global Centroid-Moment-Tensor (CMT) data (Dziewonski et al., 1981; Ekström et al., 2012). Numbered red circles represent the epicenters for destructive events in this region with (1) 1946 Chatkal earthquake, (2) 1992 Suusamyr earthquake, (3) 1885 Byelovoda (Belovod) earthquake, (4) 1887 Verny earthquake, (5) 1911 Chon-Kemin earthquake, (6) 1889 Chilik earthquake, (7) 1812 Nilke earthquake, and (8) 1906 Manas earthquake (Ainscoe et al., 2019; Dziewonski et al., 1981; Kalmeteva et al., 2009; Tsai et al., 2021; Yin et al., 2006). (b) The Dzhungarian Fault (DZF), the Lepsy Fault (LPF), and other active structures in the northern Tien Shan with GPS velocity vectors with respect to Eurasia from Zubovich et al. (2010). Red lines are the mapped surface ruptures in this study. Points *X* and *Y* are the boundaries for the three main sections (NW, central and SE) of the DZF defined by Campbell et al. (2013). The coverage of the Pléiades satellite images used in our study extends from points *X* to *Z*. Blue squares are the major cities within the area. KTF, Karatau Fault; DHF, Dzhalair-Naiman Fault; AKF, Aktas Fault; DZF, Dzhungarian Fault; TFF, Talas-Fergana Fault.



19449194, 2022, 10, Downloaded from https://agupubs.onlinelibrary.wiley.com/doi/10.1029/2022TC007300 by Test, Wiley Online Library on [10/01/2023]. See the Terms and Conditions (https://onlinelibrary.wiley.com/terms-and-conditions) on Wiley Online Library for rules of use; OA articles are governed by the applicable Creative Commons License

10.1029/2022TC007300

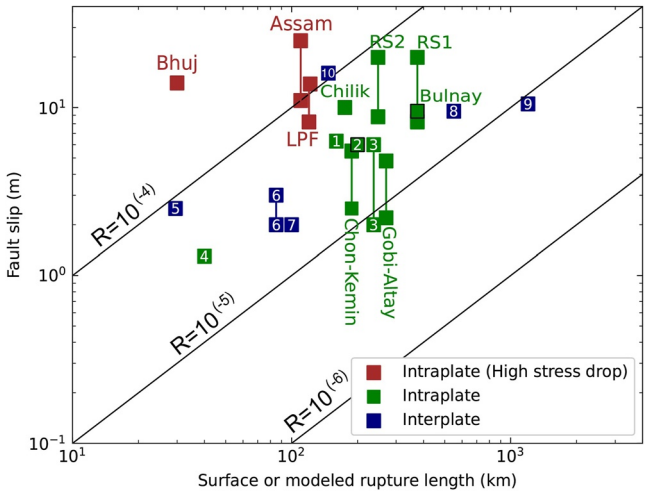


**Figure 2.** Earthquake scaling for fault slip (averaged or from minimum to maximum) against surface or modeled rupture length with slip-to-length ratio ($R$) plotted for $10^{(-4)}$, $10^{(-5)}$, and $10^{(-6)}$. Great intraplate and several renowned interplate historical earthquakes are presented along with the proposed two rupture scenarios in this study. High stress drop intraplate are labeled in brown for the 1897 Assam ($M_w$ 8.1), the 2001 Bhuj ($M_w$ 7.6), and the single Lepsy Fault rupture (LPF) ($M_w$ 8.1–8.2) (Bilham & England, 2001; Campbell et al., 2015; Negishi et al., 2002). High-magnitude intraplate events and the proposed two rupture scenarios (RS1 and RS2) are labeled in green and are highlighted by their names on the 1889 $M_w$ 8.0–8.3 Chilik, the 1905 $M_w$ 8.2–8.5 Bulnay, the 1911 $M_w$ 7.8–8.0 Chon-Kemin, the 1957 $M_w$ 8.1 Gobi-Altay earthquakes (Abdrakhmatov et al., 2016; Arrowsmith et al., 2017; Krüger et al., 2017; Kulikova & Krüger, 2015; Kurtz et al., 2018; Rizza et al., 2015). Other intraplate events (green) and renowned interplate (blue) are labeled by numbers for (1) the 1931 Fuyun ($M_w$ 7.9), (2) the 2013 Balochistan ($M_w$ 7.7), (3) the 1920 Haiyuan ($M_w$ 7.9), (4) the 1967 Mogod ($M_w$ 7.1), (5) the 2010 Darfield ($M_w$ 7.1), (6) the 1992 Landers ($M_w$ 7.3), (7) the 1999 Chi-Chi ($M_w$ 7.6), (8) the 2005 Sumatra ($M_w \sim 9$), (9) the 2011 Tohoku ($M_w \sim 9$), and (10) the 1855 Wairarapa earthquakes (Avouac et al., 2014; Bollinger et al., 2021; Catherine et al., 2005; Klinger et al., 2011; Ma & Mori, 2000; Ou et al., 2020; Quigley et al., 2012; Rodgers & Little, 2006; Satake et al., 2013; Sieh et al., 1993).

earthquakes in the Tien Shan and surroundings are recorded in detail (e.g., Kondorskaya & Shebalin, 1977; Mushketov & Orlov, 1893; Seismological Bureau of Xinjiang, 1985), meaning that the identification and mapping of ruptures is of importance in extending the record further back in time (e.g., Campbell et al., 2019; Grützner et al., 2017a).

A particularly striking single-event earthquake rupture is described by Campbell et al. (2015) on the Lepsy Fault, which is an oblique right-lateral and reverse fault in the Kazakh Platform (Figure 1b). The Lepsy ruptures are notable for their size, with slip of up to 14 m, and an unusually large slip-to-length ratio, given the mapped length of 120 km (Figure 2). The measurements of slip, length, and an assumption that rupture extended to a maximum depth of 35 km were used to estimate a magnitude in the range $M_w$ 7.5–8.2. The Lepsy Fault branches westwards from the Dzhungarian Fault. The Dzhungarian Fault is a ~300-km-long right-lateral strike-slip fault and one of the major structures in the eastern Tien Shan region (Figure 1). Campbell et al. (2013) interpreted a single-event rupture along one ~30-km section of the northern part of the Dzhungarian Fault, but suggested that the remainder of the fault no longer retains clear evidence for slip in the most recent surface-rupturing event.

In the following sections, we undertake a new analysis, using the morphology of the scarps, of the Lepsy rupture, and examine the evidence for its continuation onto the neighboring Dzhungarian Fault. We assess the distribution of slip in single and cumulative event offsets along the length of the Dzhungarian Fault, using a combination of Pléiades satellite imagery (https://www.intelligence-airbusds.com/imagery/constellation/pleiades/), digital elevation models (DEMs) derived from the satellite imagery and from field-based structure-from-motion surveys, and field measurements and sample collection. We estimate the slip vector and net slip of the most recent event from the mapped surface ruptures, and propose possible rupture scenarios of paleo-earthquakes based on fault segmentation and displacements. Finally, we discuss the coseismic rupture pattern in terms of its implication for seismic hazard and earthquake scaling relationships within intracontinental regions.

## 2. Tectonic Background

The Tien Shan is the longest mountain range in Central Asia, extending east-west for 2,500 km between longitudes 70°E to 90°E. It has experienced two major orogenic processes, with the first occurring in the Late Paleozoic and the second, ongoing, phase beginning in the Cenozoic (Windley et al., 1990, 2007). The majority of the E-W parallel ranges which make up the Tien Shan are composed of the Precambrian and Paleozoic metamorphic and structurally deformed igneous rocks resulting from the amalgamation of island arc terranes during the Late Paleozoic Variscan/Hercynian orogeny (Burtman, 1975; Voytovich, 1965). After a relatively quiescent tectonic environment during the Mesozoic, the India-Eurasia collision reactivated the Late Paleozoic structures and has resulted in significant surface deformation since ~25 Ma (Abdrakhmatov et al., 2001; Avouac et al., 1993; De Grave et al., 2007; Molnar & Tapponnier, 1975; Tapponnier & Molnar, 1979). This latest phase of orogenesis is thought to have started in the late Oligocene in the west and central Tien Shan, whereas the onset of mountain building in the northern Tien Shan occurred later, in the Miocene (Abdrakhmatov et al., 2001; De Grave et al., 2007; Hendrix et al., 1992; Windley et al., 1990). The Tien Shan is bounded to the south by the Tarim Basin and to the north by the Kazakh Platform and Dzhungarian Basin. A wide fold-and-thrust belt runs along the southern margin of the range (Burchfiel et al., 1999; Burtman, 2008; Sloan et al., 2011), whereas the northern margin is typified by basement-cored steep reverse faults (e.g., Selander et al., 2012; Wang et al., 2004). The range interior contains several fault-bounded intermontane basins (e.g., Issyk-Kul Basin) filled with up to 10 km of Cenozoic sediments



19449194, 2022, 10, Downloaded from https://agupubs.onlinelibrary.wiley.com/doi/10.1029/2022TC007300 by Test, Wiley Online Library on [10/01/2023]. See the Terms and Conditions (https://onlinelibrary.wiley.com/terms-and-conditions) on Wiley Online Library for rules of use; OA articles are governed by the applicable Creative Commons License

19449194, 2022, 10, Downloaded from https://agupubs.onlinelibrary.wiley.com/doi/10.1029/2022TC007300 by Test, Wiley Online Library on [10/01/2023]. See the Terms and Conditions (https://onlinelibrary.wiley.com/terms-and-conditions) on Wiley Online Library for rules of use; OA articles are governed by the applicable Creative Commons License

(Figure 1a; Hendrix et al., 1992). Strike-slip faults are also widespread within the Tien Shan, with left-lateral faults parallel to the range, and NNW-SSE trending right-lateral faults cutting obliquely through it. Two of the most prominent right-lateral faults are the Talas-Fergana and Dzhungarian Faults (Figure 1a). The Talas-Fergana Fault has a late Quaternary slip rate of 2.2–6.3 mm/yr (Rizza et al., 2019) and the Dzhungarian Fault slips at 1.4–4.6 mm/yr (Campbell et al., 2013; England & Molnar, 1997; Hu et al., 2021; Voytovich, 1969).

Permanent and campaign GNSS velocity measurements show the western Tien Shan accommodates 15–22 mm/yr of the current convergence, which is half the total shortening rate measured across the whole India-Eurasia collision. The rate of shortening decreases eastwards, whereas range-parallel left-lateral shearing increases (Abdrakhmatov et al., 1996; Zubovich et al., 2010). GNSS data and geological investigation indicate that N-S shortening is accommodated by active E-W reverse structures, both at the margins and within the interior, of the range (e.g., Thompson et al., 2002). The major right-lateral strike-slip faults that cut obliquely through the Tien Shan, such as the Talas-Fergana and Dzhungarian Faults, may also accommodate some shortening by rotation around a vertical axis (Campbell et al., 2013; Rizza et al., 2019; Wu et al., 2021). About 1–3 mm/yr of shortening is observed across the Dzhungarian Alatau, which is a mountain range north of the main Tien Shan (Figure 1b). Approximately 2 mm/yr of shortening is accommodated north of the mountainous regions, within the Kazakh Platform (Abdrakhmatov et al., 1996; Zubovich et al., 2010).

A number of destructive earthquakes have occurred within the last two centuries within and around the Tien Shan (Kalmeteva et al., 2009), with the causative faults and source parameters constrained to varying degrees. These earthquakes include the 1812 $M$ 8.0 Nilke (Wu et al., 2020; Yin et al., 2006) and the 1906 $M_w$ 7.7 Manas (Zhang et al., 1994) earthquakes adjacent to the Borohoro Shan in the eastern parts of the Tien Shan (Figure 1). The northern margin of the Tien Shan, including regions close to the cities of Bishkek and Almaty, were damaged by a number of events starting with the 1885 Byelovoda ($M$ 6.9) earthquake, with an epicentral zone west of Bishkek (Molnar & Ghose, 2000), and then continuing with the 1887 Verny earthquake ($M$ 7.3), which caused damage and widespread landsliding west of Almaty (Hay, 1888), the 1889 Chilik earthquake ($M_w$ 8.0–8.3; Krüger et al., 2017), and the 1911 Chon-Kemin earthquake ($M_w$ 8.0; Arrowsmith et al., 2017; Bogdanovich et al., 1914; Delvaux et al., 2001; Kulikova & Krüger, 2015). More westerly parts of the Tien Shan have produced the 1946 Chatkal earthquake ($M$ 7.6; Simpson et al., 1981) and the 1992 Suusamyr ($M_w$ 7.2) earthquake (Ainscoe et al., 2019; Ghose et al., 1997). Of all these earthquakes, only the 1911 and 1992 have ruptures that were identified and mapped by contemporary sources (Ainscoe et al., 2019; Arrowsmith et al., 2017), though probable ruptures from the 1812, 1889, and 1946 earthquakes have also been found (Abdrakhmatov et al., 2016; Simpson et al., 1981; Wu et al., 2020). There are relatively few large instrumentally recorded earthquakes adjacent to the Dzhungarian Alatau (Figure 1), and yet there is abundant evidence of significant surface-rupturing events in the prehistoric past (Cording et al., 2014; Hu et al., 2021; Shen et al., 2011; Yang & Shen, 2000), including 120 km of surface rupture with ~8–14 m slip along the Lepsy Fault (Campbell et al., 2015) and 70 km of surface rupture with 8 m slip near Tekes (Rogozhin et al., 2015; Yang et al., 1988; Figure 1a), both of which have been suggested as the potential source of a large earthquake in 1716 (Mushketov & Orlov, 1893).

## 3. Methods

### 3.1. Image Processing and Field Acquisition

We combined both remote-sensing and field-based measurements of surface ruptures. We mapped the faults and measured the surface displacements using open-source imagery hosted on Google Earth (https://earth.google.com/) and Bing Maps (https://ge-map-overlays.appspot.com/bing-maps) as well as commercial Pléiades optical satellite data in a strip along the Dzhungarian Fault. We analyzed the terrain using the 8-m-resolution High Mountain Asia (HMA) DEM provided by the National Aeronautics and Space Administration (NASA) (Shean, 2017), which covers the part of our study area west of 81.8°E and south of 46°N and was used for the first time to investigate the surface ruptures along the Lepsy Fault. We also produced meter resolution DEMs from stereo Pléiades satellite images along the Dzhungarian Fault. We produced decimeter resolution DEMs of key field sites from photographs taken in the field during unmanned aerial vehicle (UAV) field surveys. All imagery and topographic data sets are archived as outlined in our data availability statement.

Fifteen patches of bistereo Pléiades optical images were acquired during the snow-free season in May 2016, June 2016, and June 2019. These satellite images totally cover >1,350 km$^2$ with a 270-km length from 46.1°N to

19449194, 2022, 10, Downloaded from https://agupubs.onlinelibrary.wiley.com/doi/10.1029/2022TC007300 by Test, Wiley Online Library on [10/01/2023]. See the Terms and Conditions (https://onlinelibrary.wiley.com/terms-and-conditions) on Wiley Online Library for rules of use; OA articles are governed by the applicable Creative Commons License

44.4°N and a ~5-km width across the Dzhungarian Fault. Each patch has a pair of acquisitions from two different aspects and both contain a 0.5-m resolution panchromatic band and four 2-m resolution multispectral bands (Red, Green, Blue, Near Infrared). We constructed high-resolution DEMs and orthorectified imagery using the Leica Photogrammetry Suite built in Erdas Imagine software via the following procedure (Ainscoe et al., 2019; Middleton et al., 2015; Zhou et al., 2015). First, dozens of tie points were identified both manually and automatically on the pairing panchromatic images to resolve the relationship between the image coordinates and the ground coordinates. Second, pixel-by-pixel matching was implemented for the two images. Third, we used the Enhanced Automatic Terrain Extraction tool with the 3-D point positions determined from the previous steps to extract the point clouds. Fourth, the resulting point clouds were gridded at 1-m spacing. Finally, the panchromatic images and the DEMs were used to produce pan-sharpened orthorectified multispectral images which we used in our mapping.

Field surveys were conducted between July and September in 2015, 2016, and 2019 at individual sites along the Dzhungarian Fault. We collected low-altitude aerial photographs taken by a digital camera attached to the bottom of a DJI Phantom 4 quadcopter at a flying altitude of 90–100 m. Artificial ground control markers were widely distributed and measured by differential GPS (dGPS) for photographic correlation and scaling in the photogrammetry processes. We generated ~10-cm resolution orthophotos and dense point clouds by using the structure-from-motion method with Agisoft Photoscan Pro software (Westoby et al., 2012). The resulting point clouds were gridded at 10-cm spacing to generate the raster DEMs.

### 3.2. Offset Measurement

To define the size of displacements from the surface ruptures, we measured both lateral and vertical offsets from the Bing Map, Google Earth and ortho-panchromatic Pléiades imagery using QGIS software (http://qgis.osgeo.org). Lateral offsets are mostly in the form of displaced stream channels. We manually measured the channel offsets because the resolution of our imagery is insufficient for the dedicated code to implement stable and high-quality measurements (Stewart et al., 2018; Zielke & Arrowsmith, 2012). We followed the methods and assumptions described in Elliott et al. (2015), with the preferred, maximum and minimum permissible lateral offsets defined from the distances across the fault between the channel thalwegs (the lowest elevation within the channel), the outer levees, and the inner levees, respectively (Figure 3a). We also categorized the measurements into three quality categories (high, medium, and low) based on the sinuosity and the sharpness of the channels (Kurtz et al., 2018). Each measurement was further incorporated as an individual probability density function (PDF) displayed as a fixed area triangle (Figure 3b) and stacked to form a cumulative offset probability distribution function, or COPD, which can be used to identify peaks in measured offset values that may result from individual earthquakes, an established methodology used in Klinger et al. (2011), Elliott et al. (2015), Kurtz et al. (2018), Ou et al. (2020), and Dodds et al. (2022). A total of 260 laterally dislocated channels were measured in this study including 179 channels along the southern part of the Dzhungarian Fault, where the slip appears to be predominantly right-lateral (see Supporting Information S1 for the detailed lateral offset data and locations).

Vertical offsets refer to the heights of the scarps across the fault. Since we do not know the precise location of the fault projection at the surface, we defined the fault position to be at the steepest point on the scarp (Campbell et al., 2015; Grützner et al., 2017a, 2017b). The scarp profiles are either measured by dGPS in the field or extracted from the structure-from-motion DEMs using the Terrain Profile Tool in QGIS, with 100–200 m-long single-tracked profiles aligned approximately perpendicular to the scarps. The boundaries between fans and scarps were defined manually by identifying the apparent change in curvature along the profiles, avoiding the undulatory features caused by erosion or collapse. We applied a least-squares linear regression to estimate gradients of the fan surface on both sides of the fault and took the offset between the two fitted lines at the fault position as the scarp height. To account for the uncertainties introduced by the image processing and the subjective selection of scarp, fan, and fault position, we applied a Monte Carlo approach. We sampled a range of points with reasonable bounds of extent on each fan surface and fault position for 10,000 times for each profile. We used standard deviation in these multicalculated offsets as our estimation of the uncertainty. Nevertheless, it should be noted that this estimation still neglects the uncertainty caused by the landform geometry and variability in scarp heights along strike (Mackenzie & Elliott, 2017), so multiple profiles were measured at each site.

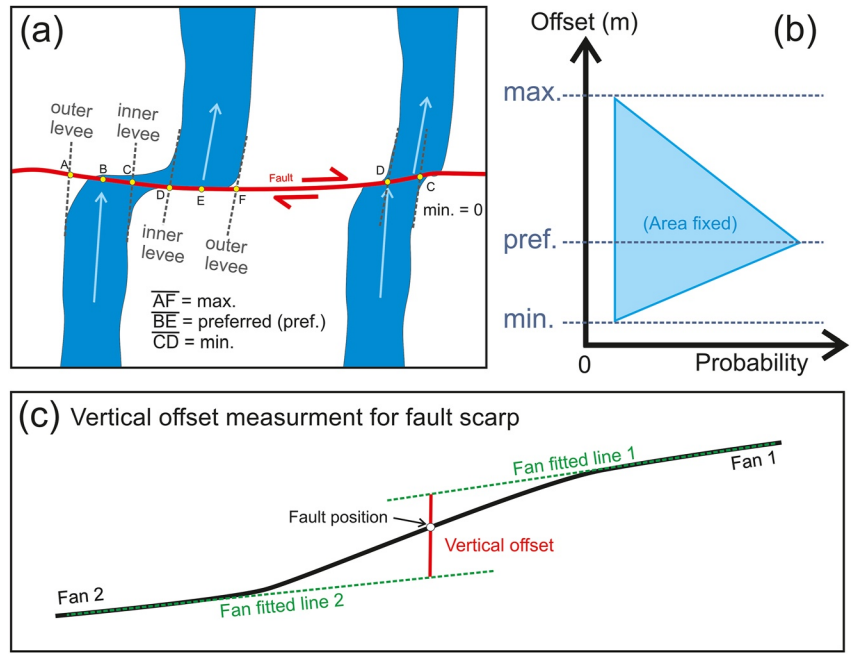


**Figure 3.** (a) Illustration of determining lateral offset measurements for stream channels estimated using satellite imagery. For each offset stream, the levees and thalweg, which is mostly at the middle of the channel, were projected to the fault. The preferred offset was assigned based upon realignment of the thalweg of the channel (distance $\overline{BE}$). Minimum ($\overline{CD}$) and maximum ($\overline{AF}$) offsets were assigned from alignment of inner and outer levees. If the preferred offset is smaller than the minimum offset, as is the case for the channel on the right, the minimum offset is set to zero. (b) Illustration of how each measurement is plotted as a triangle for demonstrating its probability density function. (c) Illustration of determining the vertical offset measurements for the fault scarps. Red line is the vertical offset estimated based on the fault position and the fan fitted lines.

### 3.3. Quaternary Dating

Age constraints on displaced terraces were obtained from radiocarbon dating of gastropod shells where such material was encountered, and through post-infrared infrared stimulated luminescence dating (post-IR IRSL) of single grains of K-feldspar from within sediment. All age data are presented in Table 1, and are archived as outlined in our data availability statement. IRSL sediment sample was collected in stainless steel tubes hammered into vertical sections of silty sediment or loess. Sample preparation was similar to that described in Grützner et al. (2017a), incorporating a density separation at 2.58 g $cm^{-3}$ applied to either 125–212 μm sieve fractions to extract K-feldspar grains. Single grain post-IR IRSL signals were measured in the luminescence laboratory at the University of Sheffield following the procedures described in Rhodes (2015) and Zinke et al. (2017). Based on previous experience from age-controlled single grain samples from Australian geoarchaeological sites (Rhodes et al., 2010), an overdispersion value of 15% was used in age estimation for all samples. No significant systematic

**Table 1**
*Radiocarbon and Infrared Stimulated Luminescence (IRSL) Dating Results*

| Radiocarbon ages | | | | | | |
|---|---|---|---|---|---|---|
| Sample name | Site | Lon. (°E) | Lat. (°N) | Materials | Calibrated range | Age (Cal. years B.P.) |
| RC1 | Bear River Site | 81.37651 | 45.90390 | Gastropod shell | A.D. 1435 to A.D. 1490 | 515–460 |
| | | | | | A.D. 1605 to A.D. 1610 | 345–340 |
| RC2 | Bear River Upstream | 81.36473 | 45.89720 | Gastropod shell | B.C. 2025 to B.C. 1885 | 3,975–3,835 |

| Luminescence ages | | | | | | | | |
|---|---|---|---|---|---|---|---|---|
| Sample name | Site | Lon. (°E) | Lat. (°N) | Depth (m) | Water (%) | Total dose rate (Gy/ka) | De (Gy) | IRSL age (ka) |
| DZH1 | Section S3 graben | 81.66034 | 45.75066 | 0.65 | 6.9 | 3.91 ± 0.24 | 66.5 ± 2.0 | 17.0 ± 1.1 |



19449194, 2022, 10, Downloaded from https://agupubs.onlinelibrary.wiley.com/doi/10.1029/2022TC007300 by Test, Wiley Online Library on [10/01/2023]. See the Terms and Conditions (https://onlinelibrary.wiley.com/terms-and-conditions) on Wiley Online Library for rules of use; OA articles are governed by the applicable Creative Commons License

19449194, 2022, 10, Downloaded from https://agupubs.onlinelibrary.wiley.com/doi/10.1029/2022TC007300 by Test, Wiley Online Library on [10/01/2023]. See the Terms and Conditions (https://onlinelibrary.wiley.com/terms-and-conditions) on Wiley Online Library for rules of use; OA articles are governed by the applicable Creative Commons License

IRSL fading was observed after assessment for every grain measured. Environmental dose rates were estimated using ICP-OES for K and ICP-MS for U and Th. Corrections were made for water content and grain size attenuation, and the dose rate estimation assumed an internal K content of 12.5 ± 2.5% (Huntley & Baril, 1997).

### 3.4. Morphological Scarp Dating

A scarp's morphology can be used to estimate its formation age. The principle of this dating technique, reviewed by Hanks (2000), can only be applied to single-event scarps and is based on the hypothesis that the scarp degrades as a simple diffusive process through time. Following this assumption, we calculated the diffusion age (kt), given in $m^2$, from the morphology of the scarp and its adjacent fan surfaces for each fault-orthogonal topographic profile. We applied a mass diffusivity of 4.19 ± 0.65 $m^2$/kyr, estimated from the nearby and climatically similar Borohoro Shan (Pang et al., 2021), to calculate how long the scarp has been going through the diffusion process. It may take hundreds of years before a scarp transitions to diffusive degradation from nondiffusive degradation processes such as slumping and collapse (Colman & Watson, 1983; Spelz et al., 2008; Wallace, 1977). At the onset of the diffusive stage, the initial scarp angle (repose angle) is assumed to be 30°–35°, meaning that scarps steeper than this angle might be relatively young (Carson & Kirkby, 1972; Nash, 1980; Pierce & Colman, 1986). In this study, we set the initial angle as 35° and implemented the morphological dating for the "likely" single-event scarps that show a clear single step without beveling along the scarps or adjacent fan surfaces, which might result from earlier scarp-forming events. Moreover, we only applied this method to the profiles from the dGPS measurements or from the drone-derived DEMs, which illustrate the scarp morphology better due to their higher image resolution, and we used the mean diffusion age averaged from multiple scarps to define the diffusion age at each investigated site (Figures S2–S7 in Supporting Information S1; Grützner et al., 2017a; Walker et al., 2017).

## 4. Geomorphology of the Dzhungarian Alatau and the Major Boundary Faults

The Dzhungarian Alatau is a roughly east-west oriented mountain range geographically separate from, though tectonically related to, the eastern Tien Shan (Figure 1a). It has an overall asymmetry with steep relief at its southern and eastern margins, with a maximum of 2,000 m relief above the surrounding sedimentary basins, and gradually diminishing relief to the west and north. The mountain summits preserve an extensive peneplain surface, which is incised by deep E-W canyons. Offsets and folding of the peneplain surface indicate the presence of reverse faulting within the range interior (Campbell et al., 2013). The east-west ridges of the Dzhungarian Alatau are bounded by reverse faults, though right-lateral strike-slip faults with orientation NNW-SSE to NW-SE are also present, either bounding the edges of the high topography, as is the case for the Dzhungarian Fault, or cutting through the range interior (Figure 1b).

The Dzhungarian right-lateral fault, also known as the Bolokenu-Aqikekuduk (or Bo-A) Fault in Chinese literature, runs along the boundary of the northern Tien Shan and the southwestern Dzhungarian Basin, straddling the border of Kazakhstan and China. The Dzhungarian Fault has existed since at least mid-Paleozoic as a structure dividing the Hercynian tectonic zones and it has been reactivated since the Late Cenozoic as a dextral strike-slip fault with reverse slip component (Campbell et al., 2013; Voytovich, 1965). The fault is ∼400-km long, and extends from the east of Lake Balkhash, Kazakhstan, in the north to the Borohoro Shan, China, in the south. It trends NNW-SSE in its southern part, and NW-SE in the north. It separates the Dzhungarian Alatau mountains and the western margin of the Dzhungarian Basin, and runs along the western side of the Dzhungarian Gate, a major low-level pass through the ranges of the eastern Tien Shan.

The Dzhungarian Fault has been separated into three main geomorphological sections by Campbell et al. (2013 Figure 1b). The northwestern section is the NW ∼150 km low-relief portion north of Usharal Town within the Kazakh Platform. The central section is the ∼160-km portion truncating the eastern margin of the Dzhungarian Alatau, with a ∼20° gradual change in strike near Lake Alakol. Oblique slip components with reverse and strike-slip components separated onto two subparallel branches are found in this central section (Campbell et al., 2013) and there is relief of ∼2,000 m across the fault. The southeastern section extends for ∼90 km across the basin of Lake Ebinur to the margin of the Borohoro Shan. There is very little relief (∼10 m) across the fault in the Ebinur basin, suggesting that the kinematics are almost purely strike-slip. The Dzhungarian Fault ends in the SE either within the Borohoro Shan, as shown in our maps, or continues through the Borohoro Shan to end in the Turfan depression (e.g., Hu et al., 2021; Shen et al., 2011; Yang & Shen, 2000). Shen et al. (2011) and Hu

19449194, 2022, 10, Downloaded from https://agupubs.onlinelibrary.wiley.com/doi/10.1029/2022TC007300 by Test, Wiley Online Library on [10/01/2023]. See the Terms and Conditions (https://onlinelibrary.wiley.com/terms-and-conditions) on Wiley Online Library for rules of use; OA articles are governed by the applicable Creative Commons License

et al. (2021) estimate slip rates of ~5 mm/yr during the last 300 ka and 3.2 + 1.4/−1.1 mm/yr during the last 100 ka, respectively, in the southern portion of the fault, in China, and Campbell et al. (2013) estimate a slip rate of 2.2 ± 0.8 mm/yr during the last 26 ka at the southern end of the central section, just north of the Kazakh border, where a long-term slip rate of 3 ± 1 mm/yr is also estimated from a 7 km offset of Pliocene-age deposits (England & Molnar, 1997; Voytovich, 1965). In this study, we examine the Dzhungarian Fault from its northern end to where it enters the Borohoro Shan. We separate the fault into eight sections mainly based on the geomorphological characteristics and the unique property within each section, as described in Section 5.2 in detail.

The Lepsy Fault has an approximate 110° strike and extends from the Dzhungarian Alatau into the low-relief Kazakh Platform. It dips ~50° to the south and possesses both reverse and dextral slip components, with a slip-vector azimuth of 317°–343° (Campbell et al., 2015). The eastern part of the Lepsy Fault, close to the Dzhungarian Fault, of the Lepsy Fault shows a clear long-term expression of faulting, with uplift to the south. West of the Shynzhyly River, where the fault enters the low-relief Kazakh Platform, there is only a very subtle long-term expression of faulting in the geomorphology. Fresh paleo-earthquake ruptures extend for the entire ~120 km mapped length of the Lepsy Fault (Campbell et al., 2015). We provide additional mapping and description of these ruptures in Section 5.1.

## 5. Paleo-Earthquake Ruptures on the Lepsy Fault and the Dzhungarian Fault

### 5.1. The Lepsy Fault

The 120-km length of ruptures along the Lepsy Fault are separated into east, central, and west sections, with the boundaries at the Shynzhyly (Shingildy) River and the Tentek River (Campbell et al., 2015; Figure 4a). The vertical displacement is easily recognized along the entire fault length whereas the significant right-lateral component is only apparent in a few locations in the eastern and central sections. The eastern section of the Lepsy Fault is sited within relatively high mountainous topography of the Dzhungarian Alatau. Campbell et al. (2015) visited the eastern section near Jaxa-Kol Lake (Figure 4a). Here, a series of southward-flowing ephemeral gullies and intervening ridges have been displaced, with drainage now ponded against a north-facing scarp 9–13 m in height, and with right-lateral displacements of 4–6 m. Campbell et al. (2015) excavated a pit into one of the dry ponds formed where one of the channels has been blocked by the scarp. The base of the ponded sediment was not reached within the pit but a bulk soil radiocarbon sample from 1.05-m deep indicates that the scarp has been present in some form for at least 2,000 years. The fresh scarps can be traced eastwards on satellite imagery to longitude 81.2°E, ~10 km from the trace of the Dzhungarian Fault (Figure 4a).

The central section of the Lepsy Fault runs along the base of the Chirindy mountains, an east-west subrange of the Dzhungarian Alatau (Figure 4a). West of the Tentek River, Campbell et al. (2015) identified a 6–9-m-high scarp with ~7-m lateral offset that they inferred to result from a single earthquake, which is consistent with our own measurements of 7–10-m scarp height from terraces adjacent to the Tentek River (Figures 4a, 4c and 4d). The north-facing scarps of the Lepsy Fault continue westwards along the base of the Chirindy mountains, and are accompanied by additional discontinuous fresh scarps within the southern, uplifted, block. We measured apparent right-lateral stream offsets of 5–9 m across some of these scarps (Figures 4e–4h). Close to the western end of the central section, the Lepsy Fault bends to the south, forming a restraining bend between its central and western sections. At this transpressional bend the north-facing scarps along the range-front end, and are replaced by a south facing scarp ~5-m high that is clearly visible in the HMA DEM (Shean, 2017; Figures 4a, 4b and 4d). The HMA DEM also reveals additional steep scarps north of the main fault trace, adjacent to the transpressional bend, near the village of Kyzylashi (Figures 4a and 4b). These scarps, that were not identified by Campbell et al. (2015), reach heights of 10–15 m. We have not visited these scarps in the field, and do not know if they represent single event or cumulative displacements. The main Lepsy scarp was measured by Campbell et al. (2015) at 7.4-m high where it crosses the Shynzhyly River. Folded and thrusted tertiary sediments exposed in the uplifted southern side of the fault attest to long-term shortening. Their radiocarbon and OSL samples from river gravels uplifted in the southern, hanging-wall, of the fault suggest these deposits were uplifted at least ~5,000 years ago, though there is no direct constraint on whether the scarp here is formed from one or more earthquakes.

West of the Shynzhyly River (Figure 4a), the Lepsy ruptures cross into the low-relief steppe of the Kazakh Platform, with only subtle evidence for prior Quaternary fault movement. The fault trace is linear, trending 107°, and composed of a number of short en-echelon segments uplifted to the south, and with small sag-ponds at their ends.

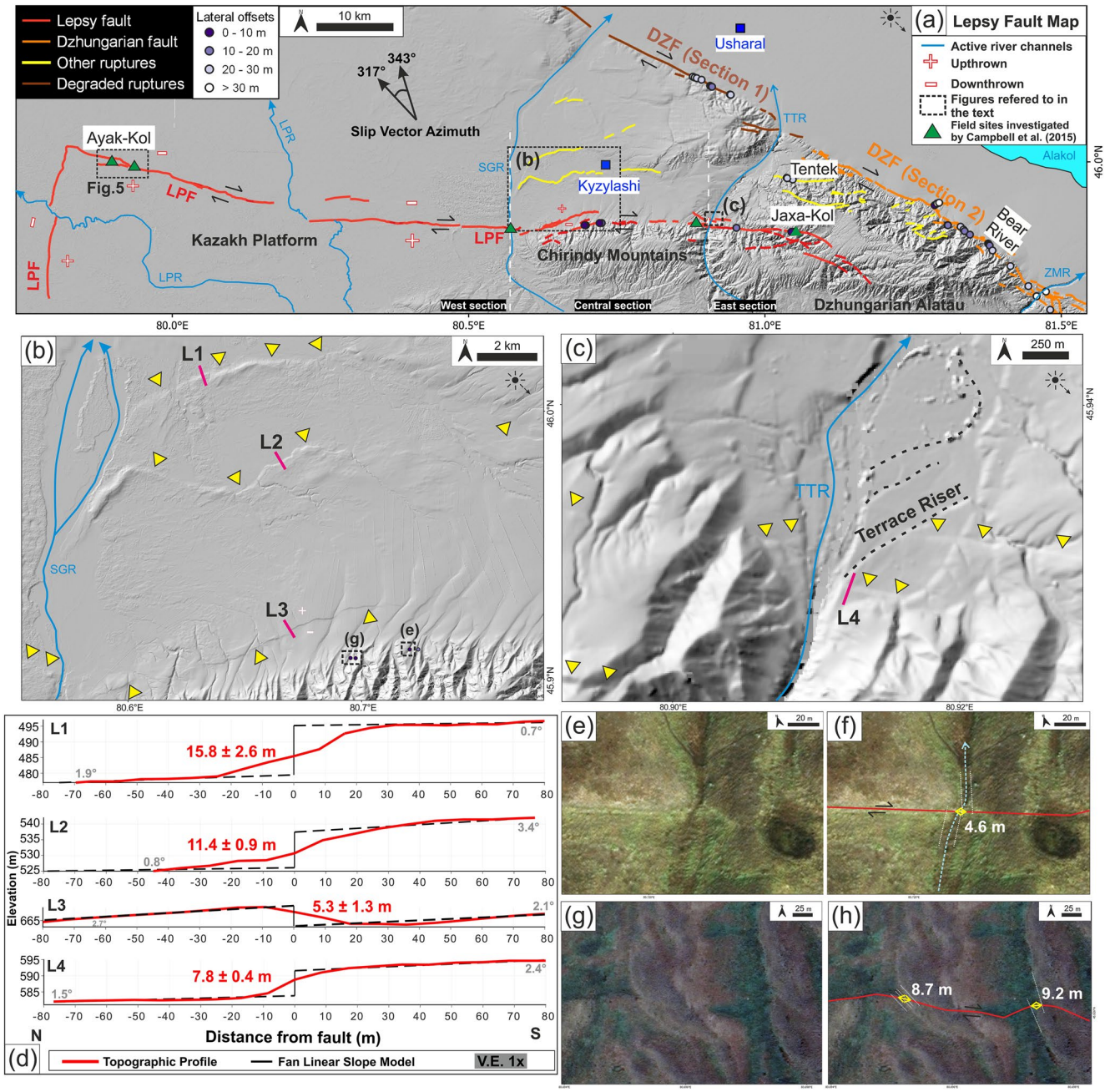


**Figure 4.** (a) Shaded-relief High Mountain Asia (HMA) digital elevation model (DEM) showing the Lepsy Fault (red) and a part of the Dzhungarian Fault (orange). "Other ruptures" include secondary fractures, lineament and other fault scarps not directly associated with the DZF and LPF. The dashed white lines separate the three main sections of the Lepsy Fault. Locations of lateral offset measurement are shown as dots. The range of estimated slip-vector azimuth of 317°–343° from Campbell et al. (2015) is shown. LPR, Lepsy River; SGR, Shynzhyly River; TTR, Tentek River, ZMR, Zhamanty River. (b) Secondary scarps in the central section of the Lepsy Fault (see "a") with the positions of three topographic profiles (L1, L2, and L3) shown by short red lines. (c) Ruptures adjacent to the Tentek River, marked by yellow arrows, with topographic profile (L4) labeled. Dotted black lines are river terrace risers. (d) Topographic profiles extracted from the HMA DEM with no vertical exaggeration (V.E. 1x). (e and g) Satellite images of the smallest lateral offset features found along the Lepsy Fault, see "b" for location, with offset values annotated in (f) and (h).

Scarp heights reach up to ~10 m (Campbell et al., 2015). At Ayak-Kol, a now abandoned and exposed channel of the Lepsy River (Figures 4a and 5) has been uplifted at the fault scarp, which it should thus predate. From radiocarbon dating of reeds and optically stimulated luminescence of cross-bedded sands forming the upper part of the exposed fluvial sequence, Campbell et al. (2015), estimate that the scarp, which is 5–7-m high at this site, formed



19449194, 2022, 10, Downloaded from https://agupubs.onlinelibrary.wiley.com/doi/10.1029/2022TC007300 by Test, Wiley Online Library on [10/01/2023]. See the Terms and Conditions (https://onlinelibrary.wiley.com/terms-and-conditions) on Wiley Online Library for rules of use; OA articles are governed by the applicable Creative Commons License

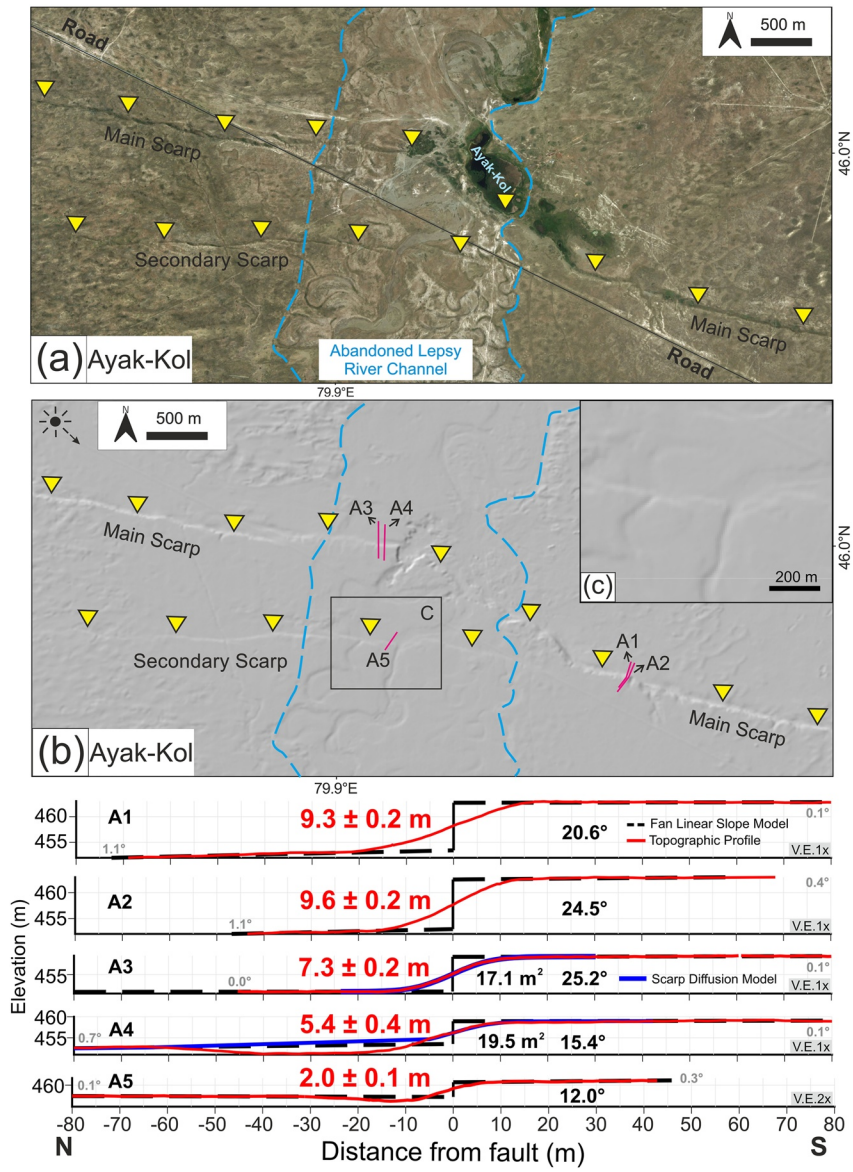


**Figure 5.** (a) Bing Map imagery and (b) shaded-relief High Mountain Asia (HMA) digital elevation model (DEM) showing the abandoned river channel (bounded by blue dashed lines) and fresh scarps (marked by yellow arrows) at Ayak-Kol (Campbell et al., 2015; Figure 4a for location). Five differential GPS topographic profiles (A1–A5) are shown below with their scarp heights (red text, in meters), maximum scarp slopes (black text, in degrees), and fan slopes (gray text, in degrees) annotated. Blue lines show the scarp diffusion model for profiles A3 and A4, the likely single-event scarps, with their diffusion ages (black text, in square meters) annotated and black lines show the fan linear slope model. Note that profile A4 have dry ponds at the base of the scarps, so those areas were excluded in estimation of the fan linear slope model. All the profiles except A5 are plotted without vertical exaggeration. (c) Close-up HMA DEM showing the secondary scarp incised by the abandoned river channel.

within the past 400 years B.P. Deeper fluvial units that have been deformed by soft-sediment deformation yielded a radiocarbon age of 5,328-4,931 calibrated radiocarbon years B.P. (Campbell et al., 2015). A second ~2-m-high scarp to the south of Ayak-Kol has been incised by the now abandoned river channel, suggesting that it formed in an earlier earthquake that predates the channel abandonment. A pit dug into the abandoned fluvial channel here yielded OSL ages of 2,245 ± 480 years and 1,810 ± 400 years B.P., which suggest may be contaminated by sands derived from older uplifted fluvial deposits exposed in the adjacent channel walls (Campbell et al., 2015). East of Ayak-Kol the two scarps merge to form a single ~9-m-high scarp, which is suggested to be a composite of two events given that the two parallel scarps are of different ages (Campbell et al., 2015; Figure 5).



19449194, 2022, 10, Downloaded from https://agupubs.onlinelibrary.wiley.com/doi/10.1029/2022TC007300 by Test, Wiley Online Library on [10/01/2023]. See the Terms and Conditions (https://onlinelibrary.wiley.com/terms-and-conditions) on Wiley Online Library for rules of use; OA articles are governed by the applicable Creative Commons License

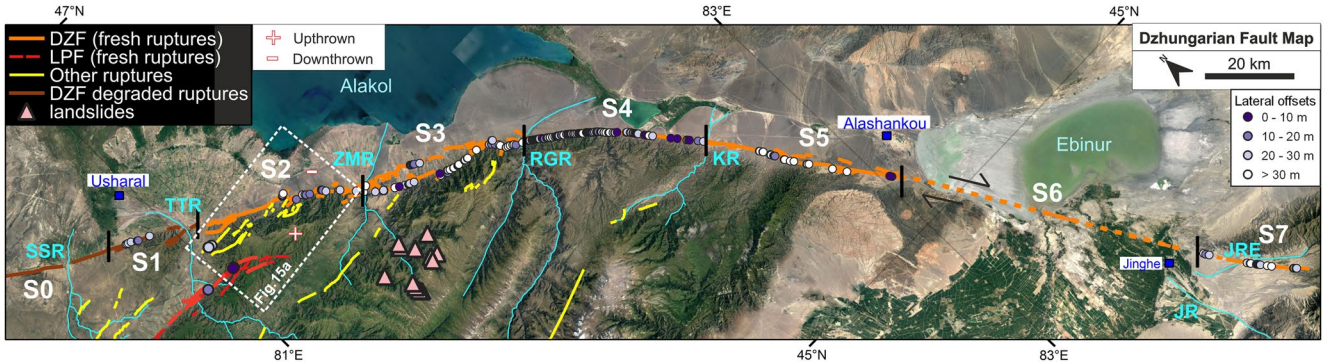


**Figure 6.** Google Earth imagery showing the Dzhungarian Fault (DZF), eastern Lepsy Fault (LPF), other ruptures (explained in Figure 4), and mapped landslides (pink triangles) within the Dzhungarian Alatau mountains (west of the DZF). Lateral offset measurements are labeled by dots. The Dzhungarian Fault is divided into eight sections from northwest to southeast (S0–S7) as represented by upright black lines with section numbers annotated. Zoomed-in images of each section are shown in Figures 7–9 and 11. Towns are marked as blue squares. SGR, Shynzhyly River; TTR, Tentek River; ZMR, Zhamanty River; RGR, Rygayty River; KR, Kokty River; JR, Jing River; JRE, Jing River East.

The age results from the Lepsy Fault are mixed from Campbell et al. (2015). In the one location (Ayak-Kol) where the geomorphology indicates a single-event scarp and has suitable material for age dating, the scarp appears to be no more than 400 years old (profiles A3 and A4 in Figure 5). At several other sites, however, there is evidence that the scarp is significantly older, with ponding against the scarp near Jaxa-Kol from at least 2,000 years ago, and 5,000-year-old fluvial sediments uplifted by the scarp at the Shynzhyly River (Figure 4a). At Ayak-Kol, there was also evidence for soft-sediment deformation of possible seismic origin affecting sediments containing organic material of age 5,328-4,931 calibrated radiocarbon years B.P. (profile A5 in Figure 5). We performed morphological scarp dating on the dGPS profiles A3 and A4, which were likely produced in a single event simultaneously, from Ayak-Kol measured by Campbell et al. (2015). These yield a mean diffusion age (kt) of 18.0 ± 0.9 $m^2$, implying they formed between 5.3 and 3.5 ka when applying a mass diffusivity of 4.19 ± 0.65 $m^2$/kyr (Pang et al., 2021; Figure 5). The morphological dating suggests a much older age than the 400 years suggested by Campbell et al. (2015), but overlapping with the ~5,000-year ages found from the Shynzhyly River and from older sediments at Ayak-Kol.

### 5.2. The Dzhungarian Fault

We divide the Dzhungarian Fault into eight sections based on the geomorphological characteristics, fault continuity, the width of fault zone, the freshness of surface ruptures, and the distribution of offsets (Figure 6), as described in Table 2. The fault geomorphology and sense of slip vary along strike with a gradual change from

**Table 2**
*Characteristics of Sections S0–S7 Along the Dzhungarian Fault*

| | Type of offsets | Continuity | Strike | Length (km) | Notes |
|---|---|---|---|---|---|
| Section S0 | Vertical | Fine | 274°–300° | 140 | Degraded scarps |
| Section S1 | Vertical and lateral | Fine | 300° | 20 | Degraded scarps and cumulative lateral displacements |
| Section S2 | Vertical and lateral | Fine | 300° | 35 | Fresh scarps and many small branches |
| Section S3 | Vertical and lateral | Fine | 300°[a] | 40 | Two main branches |
| Section S4 | Mostly lateral | Good | 306°–326° | 40 | Gradual strike changing with narrow fault zone |
| Section S5 | Mostly lateral | Good | 327° | 43 | Many relay zones with several secondary faults |
| Section S6 | Mostly lateral | (Unknown) | 327°[a] | 67 | Fault traces mostly obscured by sediments and the lake/lowest topographic relief |
| Section S7 | Mostly lateral | Good | 324° | 23 | Low quality offset features |

[a]Strike of S3 is defined by the linearity connecting the end of S2 and the top of S4.



19449194, 2022, 10, Downloaded from https://agupubs.onlinelibrary.wiley.com/doi/10.1029/2022TC007300 by Test, Wiley Online Library on [10/01/2023]. See the Terms and Conditions (https://onlinelibrary.wiley.com/terms-and-conditions) on Wiley Online Library for rules of use; OA articles are governed by the applicable Creative Commons License

19449194, 2022, 10, Downloaded from https://agupubs.onlinelibrary.wiley.com/doi/10.1029/2022TC007300 by Test, Wiley Online Library on [10/01/2023]. See the Terms and Conditions (https://onlinelibrary.wiley.com/terms-and-conditions) on Wiley Online Library for rules of use; OA articles are governed by the applicable Creative Commons License

almost pure right-lateral strike-slip faulting in the southeast, where the fault trends at ~330°, to oblique slip with a substantial vertical component of motion in the northwest, where the strike is ~300°. Sections S0 and S1 extend from the south of Usharal to the northwestern end of the fault (Figure 6). The tectonic geomorphology of these two sections is noticeably different from that of Section S2 southwards, in that the fault along S0 and S1 is manifest only as degraded scarps and much of the evidence for faulting has been completely removed by fluvial erosion during the deposition of the youngest generation of alluvial fans along the range front (Figures 7c and 7d). No discrete earthquake ruptures can be identified along S0 and S1. In contrast, the scarps along S2 are well-preserved and continuous, even within the young alluvial deposits (Figures 7b, 7e and 7f). Campbell et al. (2013) inferred that the scarps along S2 were produced by a single earthquake. Here, we investigate the potential for that single-event rupture to extend much further south along the Dzhungarian Fault by at least 200 km including Section S3 which is composed of two main branches and Sections S4–S7 where the fault appears to be pure strike-slip. We also identify additional fresh scarps between the Lepsy and Dzhungarian Faults, and describe clusters of bedrock land sliding within adjacent highlands. We start our description in the south, where the fault appears to be predominantly strike-slip, before addressing the evidence for single-event slip in the more northerly and complicated oblique slip sections (S2 and S3).

#### 5.2.1. Borohoro Shan to the Rygayty River (Sections S7–S4)

From where it exits the Borohoro Shan in the south to where it crosses the Rygayty River, the Dzhungarian Fault is generally straight and continuous without major branches (Campbell et al., 2013), though it can be separated into four sections (S7–S4) based upon its geomorphological characteristics. Section S7 is defined as the part of the fault from the Borohoro Shan to Jinghe Town. In this section, the fault tracks through terraces and tributaries of the river in the east of the Jing River (named Jing River East (JRE) in this study). Most of the streams along S7 are oblique (25°–30°) to the fault, which poses challenges in measuring the precise channel offset. Vertical offsets are restricted to short transpressional and transtensional relays (Campbell et al., 2013; Hu et al., 2021). Although the laterally offset features along S7 are mostly defined as low quality, our measurements based on Pléiades imagery show the smallest offsets are around 6.9–8.4 m (Figures 8b, 8e and 8f). These values happen to be similar to the 6–9 m single-event offset interpreted by Hu (2019) from examining high-resolution drone imagery in this area and their further COPD analysis. Adjacent to the Ebinur lake basin the fault becomes hard to trace, leading us to separate this part into a separate Section S6 (Figure 8a). To the south of Lake Ebinur, the fault trace is mostly obscured by widespread agriculture. However, we recognized a linear fault trace right at the south of the shoreline and a likely pull-apart basin following the same trend in the further south (Figures 8a, 8c and 8d), which potentially have recorded the ruptures on S6. To the north of the lake the fault is visible cutting through paleo-shorelines, but there are no geomorphic features from which lateral displacements can be measured.

We defined S5 as the section of the fault from Lake Ebinur northwards to the Kokty River (Figure 9b). This section has an average strike of 327°. There are several <2-km-long pressure ridges and pull-apart basins plus some ~5-km-long subsidiary faults 2 km eastwards of the primary fault. Several high-quality laterally offset channels are found with the smallest displacement measured at 7.9 m (Figures 9i and 9j). Vertical offsets are only found within the relay zones. On the subsidiary faults, there are some <1 m vertical displacements but no lateral offsets were identified.

Section S4 runs from the Kokty River northwards to the Rygayty River (Figure 9a). Within this section, the strike of the fault gradually changes from 326° in the southeast to 306° in the northwest. Despite the strike change, the fault zone remains the narrowest (mostly <100 m) among its adjacent sections, and is well defined and continuous. Numerous and widely distributed laterally offset channels are found. Vertical displacements are restricted to small relay zones. The smallest high-quality lateral offsets along a single strand found on this section are in the range of 6.9–8.8 m (Figures 9c–9h).

Overall, the Dzhungarian Fault along Sections S7–S4, south of the Rygayty River, is relatively continuous and appears to be predominantly strike-slip, with an average slip-vector azimuth of ~328°. The smallest lateral offsets measured from a single strand along these sections are in the range of 6.9–8.8 m based on individual measurements (Figure 9). Due to the lack of historical coseismic slip data along this fault, we infer that these smallest offsets are likely to represent the slip in the most recent surface-rupturing earthquake, which is the working assumption based on the models developed for other historical earthquakes (e.g., Klinger et al., 2011; Kurtz et al., 2018). To calculate the average slip and to assess the evidence for prior offsets we produced a COPD from the stacked triangular PDF of individual offsets along the single-fault trace on Sections S4 and S5 (Figure 10),

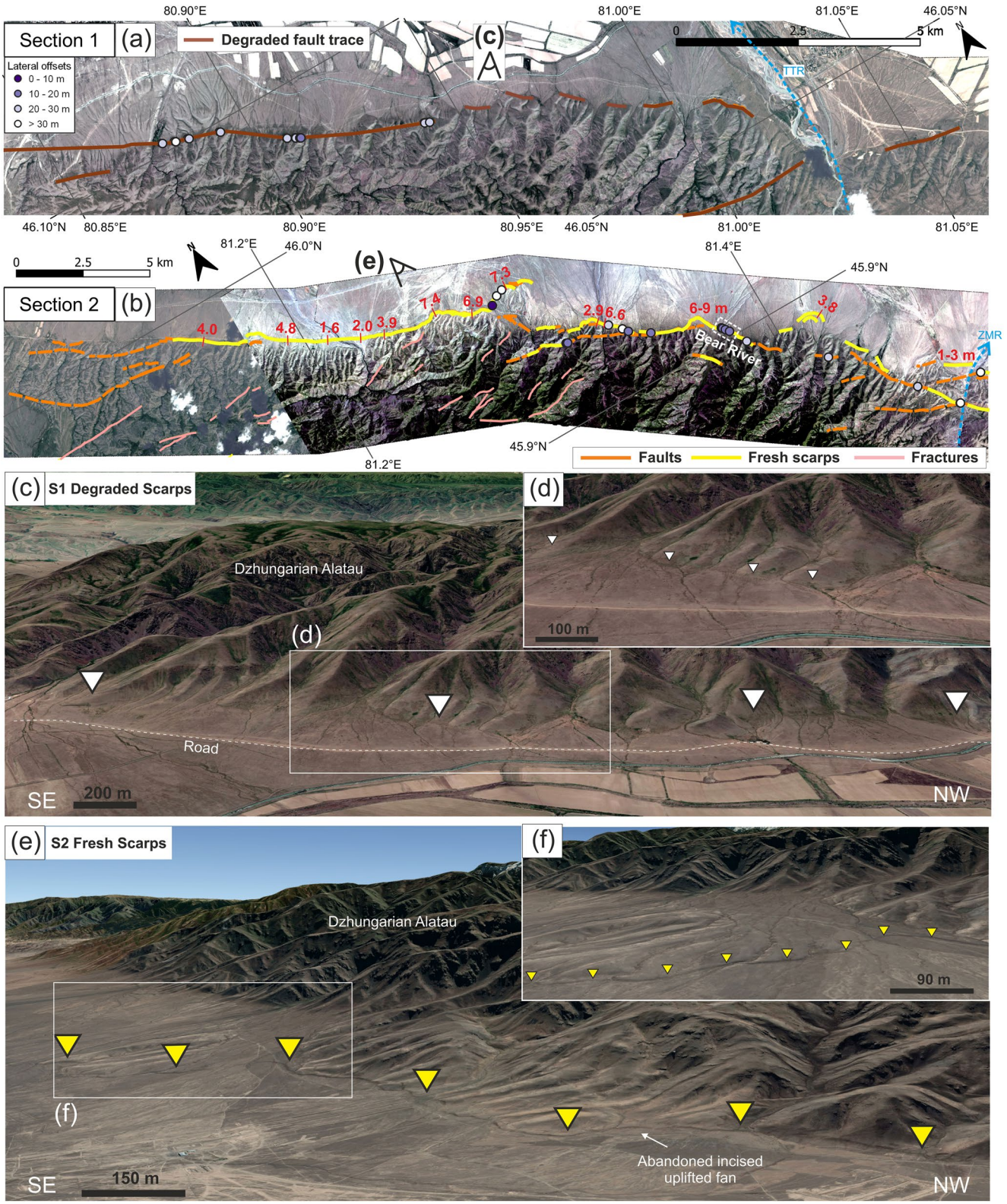


**Figure 7.** Orthorectified Pléiades imagery showing (a) Section S1 and (b) Section S2 of the Dzhungarian Fault with mapped fault traces and offsets (see Figure 6 for locations, TTR, Tentek River, ZMR, Zhamanty River). Heights of the fresh scarps are annotated in red text with short red lines showing the measured locations. (c) and (e) are Google Earth satellite images looking obliquely SW along Section S1 and Section S2 with close-up details shown in (d) and (f), respectively, showing the different level of scarp degradation and morphology at the range front between these two sections. Degraded scarps are pointed by white arrows; fresh scarps are pointed by yellow arrows.



19449194, 2022, 10, Downloaded from https://agupubs.onlinelibrary.wiley.com/doi/10.1029/2022TC007300 by Test, Wiley Online Library on [10/01/2023]. See the Terms and Conditions (https://onlinelibrary.wiley.com/terms-and-conditions) on Wiley Online Library for rules of use; OA articles are governed by the applicable Creative Commons License

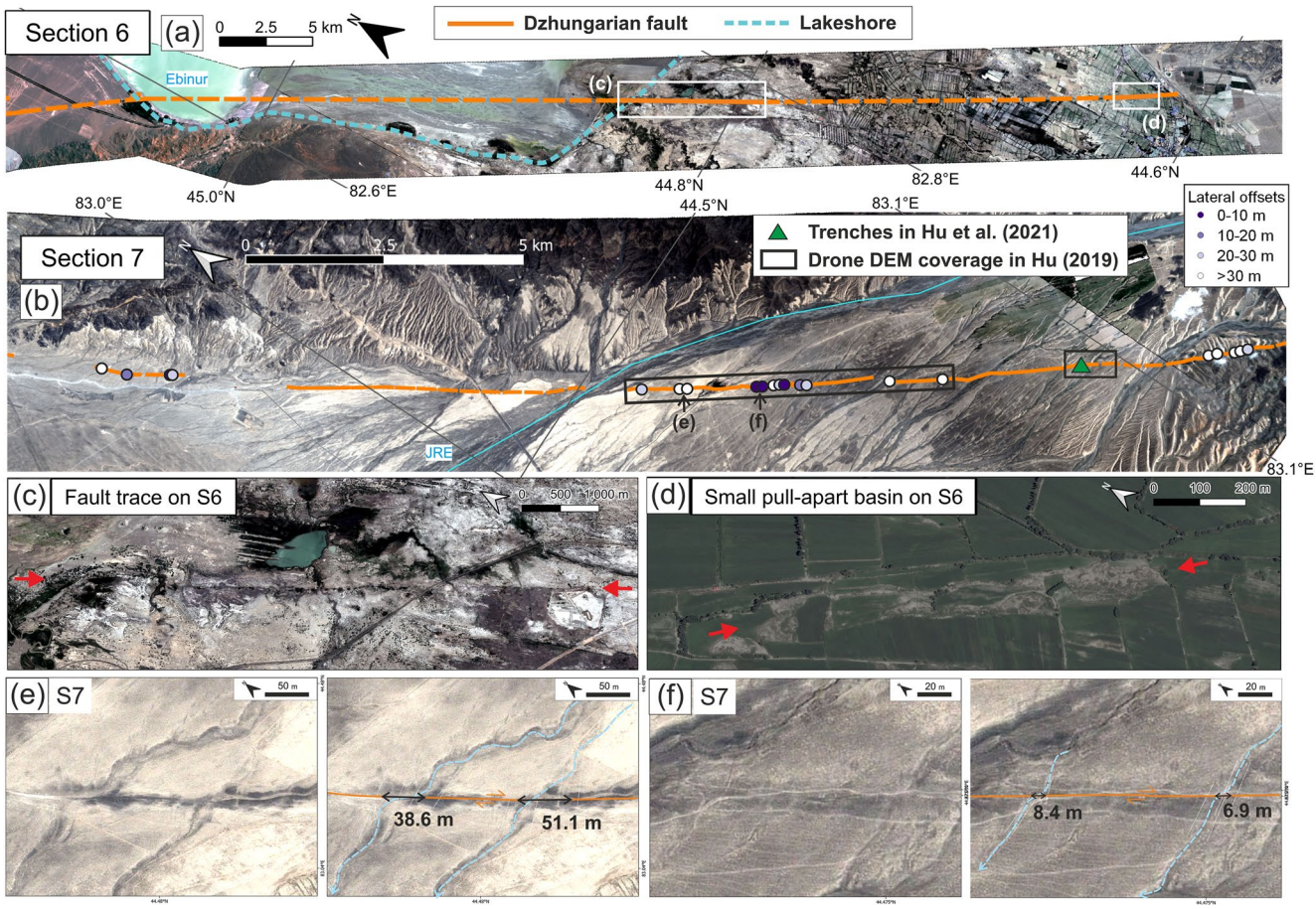


**Figure 8.** Orthorectified Pléiades imagery showing (a) Section S6 and (b) Section S7 with mapped fault traces and offsets measurement sites annotated. The maximum extent shoreline of Ebinur is shown by a blue dashed line in "a." Dashed orange lines are the inferred fault trace. (c) The linear fault trace (pointed by red arrows) at the south of the Ebinur Lake. (d) A pull-apart basin (pointed by red arrows) cutting through the fields. Locations of the trench and coverage of the high-resolution drone imagery from Hu (2019) and Hu et al. (2021) are labeled in "b." (e) and (f) are the lateral offset channels with the interpretations found along Section S7. JRE, Jing River East.

where the fault has good continuity and where the measured high-quality smallest offset values remain similar along the fault (Klinger et al., 2011; Kurtz et al., 2018; Zielke et al., 2010). The COPD plot shows three peaks at 8.8 m, 15.2, and 23.7 m, which we infer to result from slip in the three most recent earthquakes. This corresponds to slip of 8.8 m, 6.4, and 8.5 m in the most recent, penultimate and antepenultimate events, respectively (Figure 10c). Although the COPD peaks are not prominent, the inferred amounts for the past coseismic slip generally fit with the smallest lateral offsets of 6.9–8.8 m from individual measurements from the imagery.

### 5.2.2. From the Rygayty River to the Zhamanty River (Section S3)

Between the Rygayty and Zhamanty Rivers, the Dzhungarian Fault splits into two prominent branches, which is a unique geometry along this fault (Figure 11a). We defined this portion as Section S3 with an average strike of 300°. On the northern branch, vertical displacements dominate, though several apparently right-laterally offset channels are also observed (Figure 11a). The scarp along the northern branch cuts through a number of different generations of alluvial fans, with the most widespread one having a scarp of ~14-m high (Figures 11j–11l).

The southern fault branch tracks into the foothills of the Dzhungarian Alatau and appears to be predominantly right-lateral strike-slip, with abundant offsets of ridges and streams (Figures 11b and 11c). The smallest lateral offsets that we found along the southern branch are 7.3–9.2 m (Figures 11d–11i). A small (~1-km long) transtensional graben along the southern fault trace is shown in Figure 12. The south side of the graben is bounded by a north-facing steep fault scarp that displaces a low-relief alluvial surface. Five topographic profiles (B1–B5) extracted across this scarp from a drone-derived SfM digital model (Figure 12) show it to be 8–12-m high, except



19449194, 2022, 10, Downloaded from https://agupubs.onlinelibrary.wiley.com/doi/10.1029/2022TC007300 by Test, Wiley Online Library on [10/01/2023]. See the Terms and Conditions (https://onlinelibrary.wiley.com/terms-and-conditions) on Wiley Online Library for rules of use; OA articles are governed by the applicable Creative Commons License

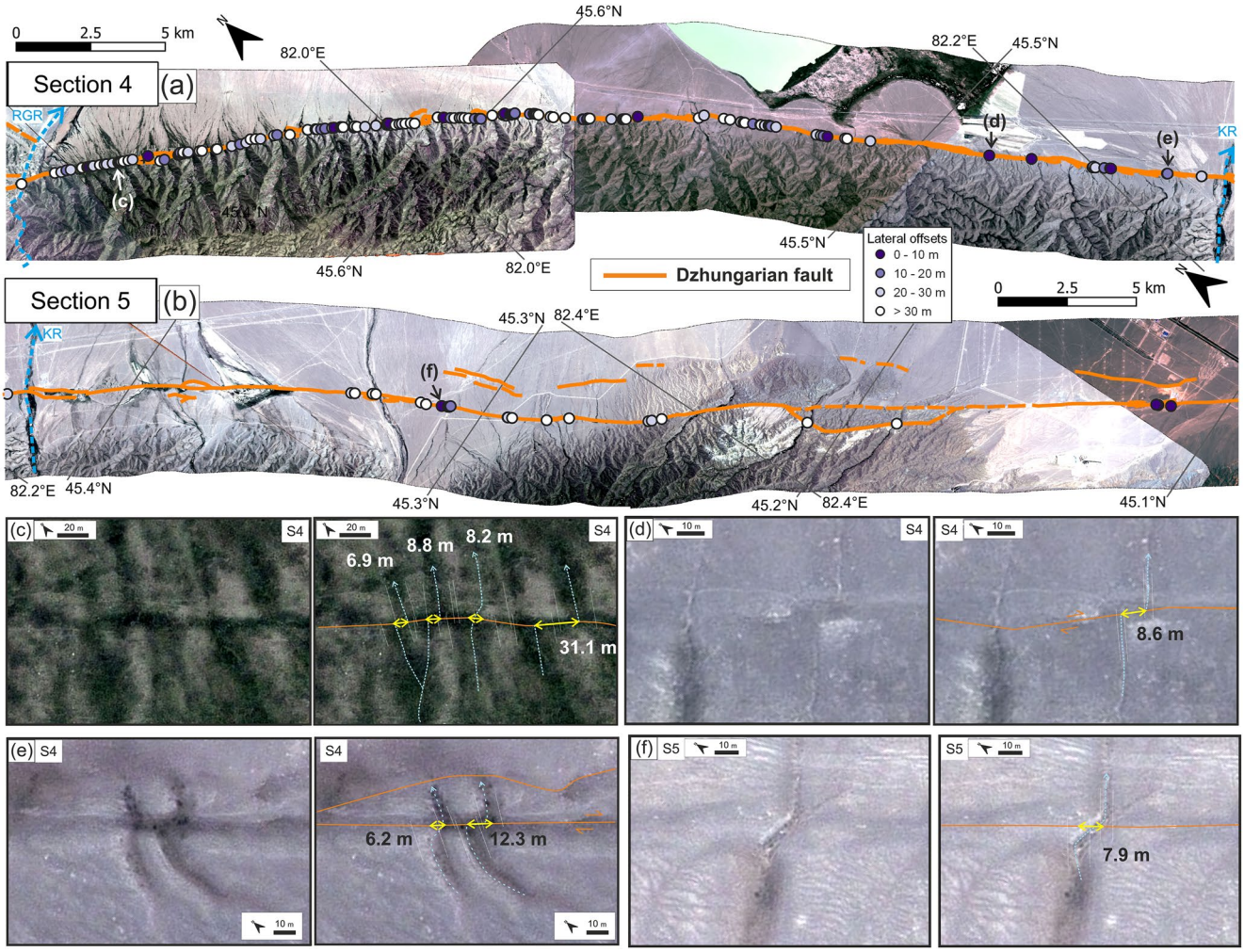


**Figure 9.** Orthorectified Pléiades imagery showing (a) Section S4 and (b) Section S5 of the Dzhungarian Fault with mapped fault traces and offset measurement sites annotated. (c–f) Close-up Pléiades imagery showing the smallest high-quality offset channels along Sections S4 and S5 with the displacements annotated in meters. Example (e) shows closely spaced probable single event and cumulative offsets. There is a second fault splay at location (e), such that the measured offset may underestimate earthquake displacement and these kinds of measurements would be excluded from the probability density plot and the cumulative offset probability density (COPD) analysis.

in Profile B4 where it is only ~6-m high. We note that Profile B4 goes across a small channel and a road on the upper fan, which might have modified the original scarp shape, though we cannot exclude an interpretation of this lower scarp value reflecting the true scarp offset. The topographic profiles show the scarp to be a single step, suggestive of a single-event rupture, though the nearby 6-m measurement might instead indicate that where the scarp is higher, it resulted from a minimum of two events. We collected a single IRSL sample (DZH1) from a loess exposure under the terrace surface on the upthrown side of the southern fault. The sample was taken at a depth of 65 cm and yielded an age of 17.0 ± 1.1 ka (Figure 12e and Table 1), which should predate the formation of the basin scarps. Morphological scarp dating, excluding Profile B4 whose original shape might be modified, yielded a mean diffusion age (kt) of 19.9 ± 3.2 $m^2$ and a scarp age of 6.5–3.5 ka (Figure 12g).

### 5.2.3. From the Zhamanty River to the Tentek River (Section S2)

Section S2 of the Dzhungarian Fault extends from the Zhamanty River in the south to the Tentek River in the north with a strike of 300°. The fault in this section has a substantial vertical component, which is accommodated along a single main oblique fault, though minor fresh scarps are also distributed within adjacent foothills (Figure 7b).



19449194, 2022, 10, Downloaded from https://agupubs.onlinelibrary.wiley.com/doi/10.1029/2022TC007300 by Test, Wiley Online Library on [10/01/2023]. See the Terms and Conditions (https://onlinelibrary.wiley.com/terms-and-conditions) on Wiley Online Library for rules of use; OA articles are governed by the applicable Creative Commons License

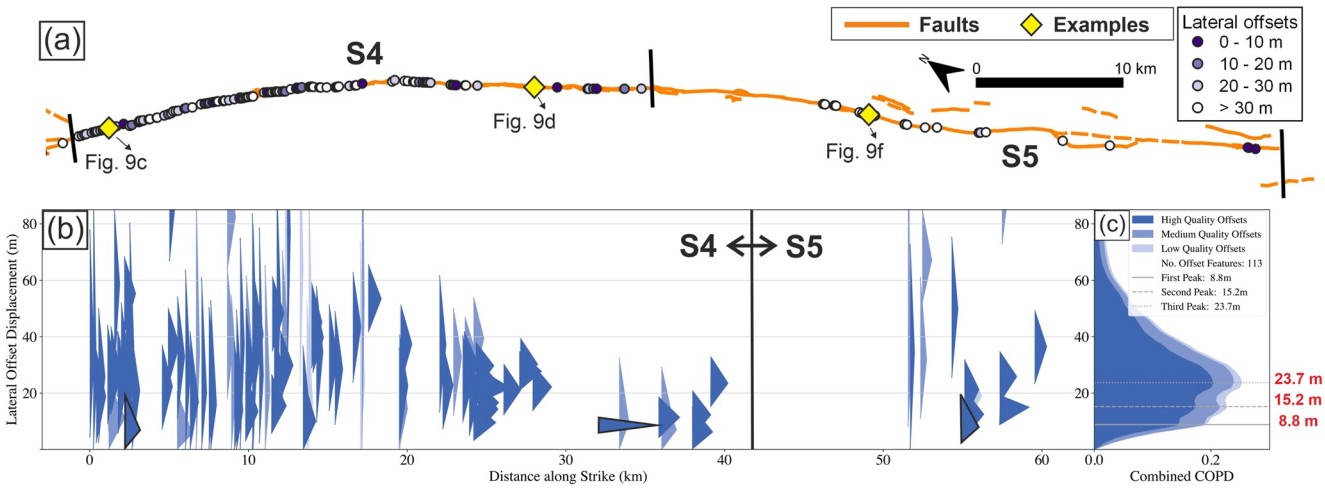


**Figure 10.** (a) Fault trace of Sections S4 and S5 of the Dzhungarian Fault. Examples of high-quality smallest offset measurements are marked by yellow diamonds and their corresponding triangular probability density functions (PDFs) framed by black lines in "b." (b) Probability density plot for the 113 dextral offset channels along the single-fault trace of S4 and S5. Each triangle represents an individual offset PDF with dark blue to light blue colors representing high to low quality of the offset measurement. (c) Stacked cumulative offset probability density (COPD) with values of the three peaks annotated in red.

The "Bear River" site (Figure 13) is important in showing the potential slip in the most recent event on the fault. The Dzhungarian Fault crosses upper (T2) and lower (T1) alluvial surfaces, adjacent to the active river terrace (labeled T0 in Figure 13c), that have been displaced obliquely by the fault. Streams on the upper surface appear to have been displaced dextrally by ~12 m, with one stream potentially showing as much as 15.7 m offset (Figure 13d). The riser between T2 and T1 is right-laterally displaced by 13 m. There are no reliable markers of lateral offset on T1, probably covered by the sedimentation in the downthrown side. Six topographic profiles extracted from a drone-derived SfM model show a single step without beveling and with similar heights, with an average of ~7.9 m, on both the older and younger terraces (Figures 13b, 13e and 13f). Profile P2 has a double scarp morphology that we infer to result from localized slumping along the scarp, as represented by dotted red lines in Figure 13c.

The similarity in scarp heights in both T1 and T2 at the Bear River site, and the similarity in right-lateral offset of streams in the T2 surface and the T1–T2 riser suggest that both terraces have experienced the same amount of displacement. Furthermore, the scarp morphologies suggest, at a qualitative level, that the displacement possibly occurred in a single earthquake event, which is also supported by the consistency in scarp height measured more widely along S2, as described earlier. Morphological scarp dating for all profiles except P2, which we excluded due to the possibility of slumping, yielded a mean diffusion age (kt) of 24.2 ± 1.8 $m^2$, implying a scarp age of 7.3–4.6 ka. On the upthrown side of the scarp, a snail sample (RC1) extracted from ~1 m below the upper terrace (T2) surface (Figure 13a) was collected and yielded radiocarbon ages of 515–460 and 345–340 calibrated radiocarbon years B.P. (Table 1).

Upstream of the main Bear River scarp, a second scarp was found with a height of 4.4 ± 0.6 m (Figures 14a and 14b). This scarp has a diffusion age (kt) of 15.9 ± 2.9 $m^2$, implying a scarp age of 5.3–2.7 ka (Figure 14b). Another snail sample (RC2) embedded within fluvial deposits at a depth of ~1 m on the upthrown, southern, side of the fault yielded a radiocarbon age of 3,975–3,835 calibrated radiocarbon years B.P. (Figures 14c and 14d, Table 1).

We measured the scarp heights along the length of S2 from topographic profiles through the Pléiades-derived DEM, primarily at sites where the scarp crosses small river catchments. We found consistent 6–9-m-high scarps for the southern 12 km of S2 (Figure 7b), including the Bear River site as described above. Occasional lower scarp heights of 1–4 m are all sited on small splays rather than the main fault. The absence of scarps <6–9 m on the main fault, despite the wide preservation of scarps and the abundance of young faulted alluvial deposits, suggests that the 6–9-m scarps were formed in a single earthquake. For the northern seven km of S2, however, the scarps abruptly reduce in height to <5-m high. Campbell et al. (2013) visited this part of the rupture and inferred



19449194, 2022, 10, Downloaded from https://agupubs.onlinelibrary.wiley.com/doi/10.1029/2022TC007300 by Test, Wiley Online Library on [10/01/2023]. See the Terms and Conditions (https://onlinelibrary.wiley.com/terms-and-conditions) on Wiley Online Library for rules of use; OA articles are governed by the applicable Creative Commons License

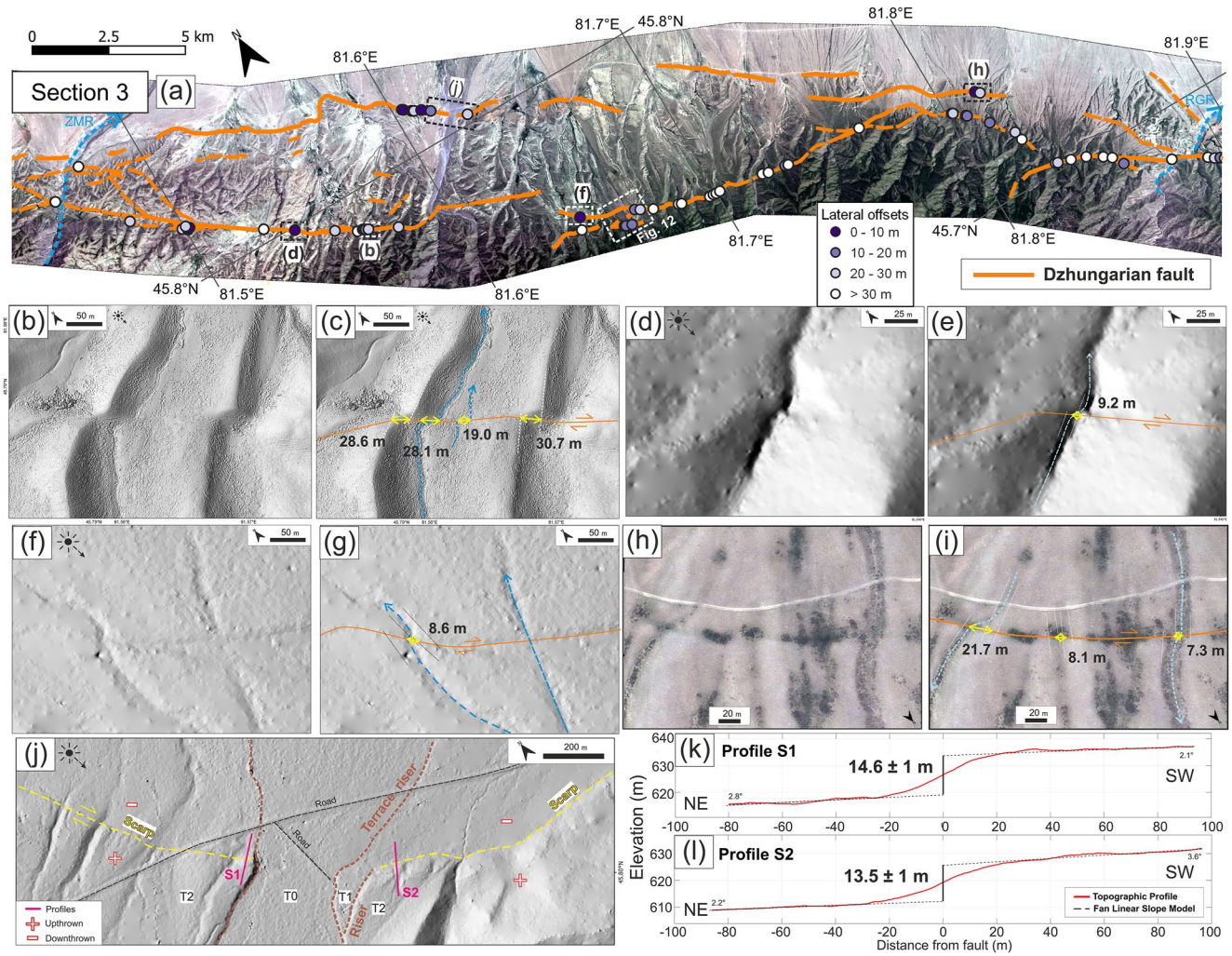


**Figure 11.** (a) Orthorectified Pléiades imagery showing Section S3 of the Dzhungarian Fault (see Figure 6 for location) with mapped fault traces and offsets measurement sites annotated. (b–i) Orthorectified and shaded-relief topography derived from Pléiades imagery of the laterally offset channels along S3 with the amounts of displacements annotated; see "a" for locations. (j) Shaded-relief topography derived from Pléiades imagery showing the terraces T2-T0, from old to young, and the ~14-m scarps along the northern fault branch, with locations of the two profiles (S1 and S2) labeled; see "a" for location. (k–l) Topographic profiles S1 and S2 from Pléiades-derived digital elevation models (DEMs) with their heights annotated.

a single-event origin of scarps measured at 1.6 ± 0.2-m high. The "fresh" scarps end at the transition from S2 to S1, with the morphology of S1 and S0, as described below, being much more subdued.

### 5.2.4. North of the Tentek River (Sections S1 and S0)

We defined S1 as the section of the fault from the Tentek River northwards to ~46.10°N with a strike of 300°. On Section S1, the total topographic relief is up to 600 m with several dextral offsets of around 20–30 m, but no fresh scarps were found (Figure S1 in Supporting Information S1). Section S0 is defined as the part of the fault north of 46.10°N. This section also generally trends 300° but it bends to the south at 46.67°N to a strike of 240°. The topographic relief on Section S0 is mostly <200 m with no fresh scarps, laterally offset features or fractures, which do not have apparent or extensive offset but have obvious linearity.

### 5.2.5. Faulting, Fracturing, and Landsliding Within the Dzhungarian Alatau Foothills

The abrupt decrease in scarp height from 6 to 9 m to <5 m within S2 coincides with significant splay faults and associated fracture that runs ENE into the Dzhungarian Alatau and exits into the lowlands east of the Tentek River, northeast of the Lepsy rupture (Figure 15a). We visited one of the splay faults at the "Tentek River East" site (Figure 15a) where we surveyed steep north-facing scarps preserved within a small stream catchment. The



19449194, 2022, 10, Downloaded from https://agupubs.onlinelibrary.wiley.com/doi/10.1029/2022TC007300 by Test, Wiley Online Library on [10/01/2023]. See the Terms and Conditions (https://onlinelibrary.wiley.com/terms-and-conditions) on Wiley Online Library for rules of use; OA articles are governed by the applicable Creative Commons License

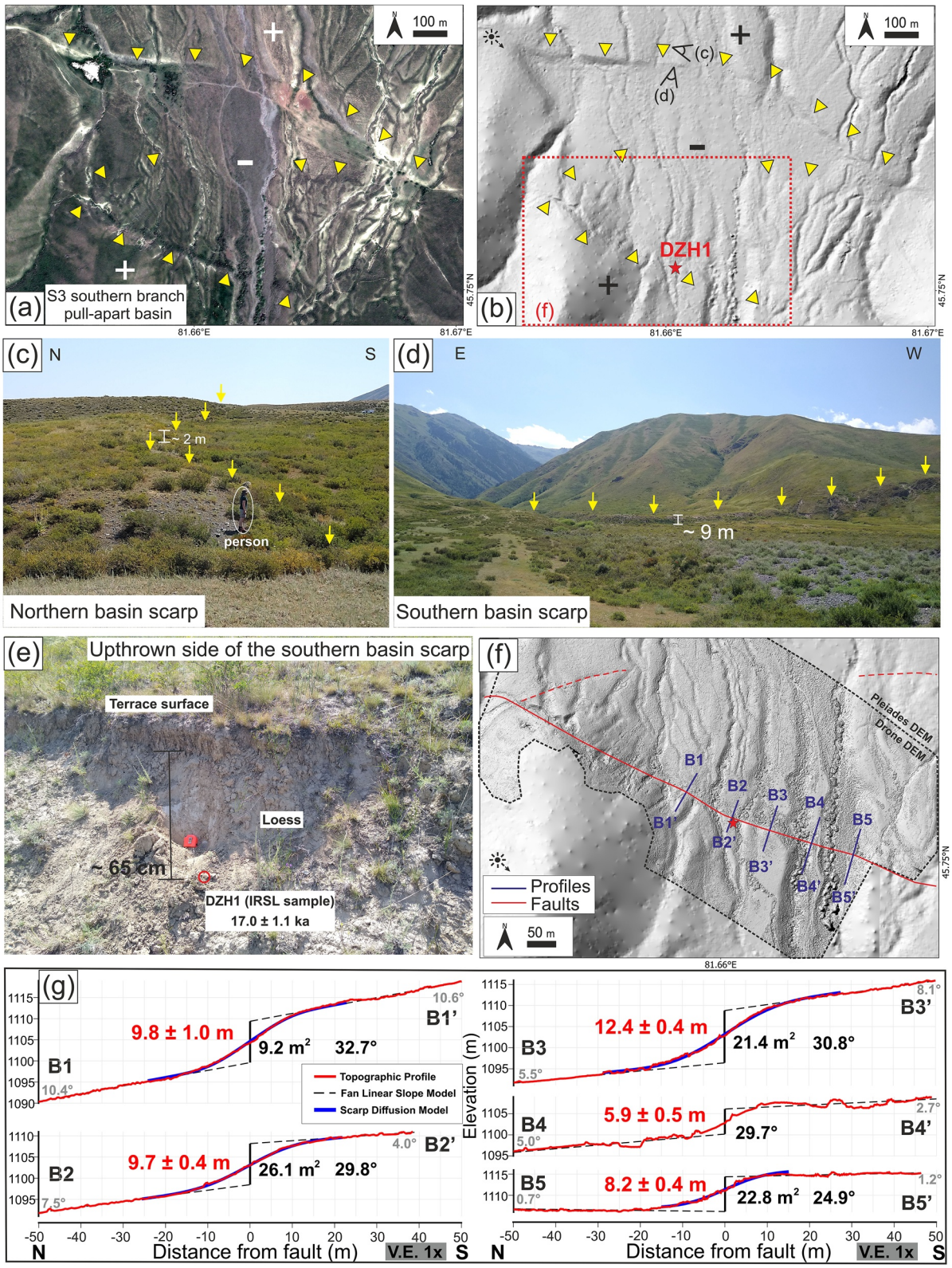


**Figure 12.**



19449194, 2022, 10, Downloaded from https://agupubs.onlinelibrary.wiley.com/doi/10.1029/2022TC007300 by Test, Wiley Online Library on [10/01/2023]. See the Terms and Conditions (https://onlinelibrary.wiley.com/terms-and-conditions) on Wiley Online Library for rules of use; OA articles are governed by the applicable Creative Commons License

present-day stream has cut a narrow gorge through the uplifted block, leaving the remainder of the scarp well preserved. The scarp height in individual topographic profiles ranges from 4.0 to 10.2 m along strike, but most heights are >8 m and all show a single topographic step without beveling, meaning they might be single earthquake displacements (Figure 15e). Features offset by >20 m could be found along these scarps. We conducted morphological scarp dating of seven profiles at this site. We found that Profile T4 has over twice the diffusion age of the others. The mean diffusion age (kt) from all profiles except T4 is 11.3 ± 1.6 $m^2$, implying a scarp age between 3.6 and 2 ka. Apart from these high and fresh fault scarps, some small and fresh fractures are also recognized at the range margins within this transition area between the Dzhungarian and Lepsy Faults (Figures 15 and 16) and are widespread within the foothills of the Dzhungarian Alatau, especially adjacent to S2 and S3 (Figure 16a). These scarps are clearly visible in the satellite imagery though we did not find any indicators of lateral offset (Figures 16b–16f). We also identify a number of large rock avalanches within the Dzhungarian Alatau adjacent to S3 (Figures 16a and 16g). The landslides have occurred on steep west and north-facing slopes, and the debris have formed small lakes within adjacent valley bottoms.

## 6. Discussion

### 6.1. Paleo-Earthquake Rupture in the Most Recent Event

We have described evidence for young geomorphic displacements that we interpret to have resulted from single earthquakes along the Dzhungarian and Lepsy Faults, along with a number of splay faults that occupy the mountainous region between them. The southern parts of the Dzhungarian Fault (Sections S7-S4) trend ∼328° and are predominantly right-lateral strike-slip. Section S3 has a trend of ∼300° and is oblique slip, with right-lateral and reverse components partitioned onto parallel structures separated by up to 6 km. Section S2 is a single oblique-slip range-front fault with splays branching westwards into the Dzhungarian Alatau. Sections S1 and S0 do not appear to have been reactivated since deposition of the youngest widespread generation of alluvial fan, which is not displaced by faulting along these sections. Campbell et al. (2015) estimated the fault slip in the eastern part of the Lepsy Fault to be 8.2–13.8 m and a slip-vector azimuth of 317°–343° from a site where they could measure both vertical and lateral components of slip, along with an independent estimate of fault dip (50°S). The similarity in slip-vector azimuth between that determined by Campbell et al. (2015) on the Lepsy Fault, and the 328° slip-vector azimuth implied by the trend of the southern Dzhungarian Fault, where the slip is predominantly right-lateral strike-slip, lead us to assume that the slip-vector azimuth is constant along the lengths of the Dzhungarian and Lepsy Faults, as is seen in other ruptures with significant strike changes such as the 2002 Denali Fault Earthquake and the 1999 Chi-Chi Earthquake (Haeussler et al., 2004; Lee et al., 2002).

To estimate the distribution of slip representing the most recent surface rupture(s) along the Dzhungarian Fault, we use different approaches in the south and north. In the south (Sections S7–S4) where the slip is predominantly right-lateral, we use high-resolution satellite imagery to identify and measure numerous stream displacements, yielding an average of 8.8 m of right-lateral displacement in the most recent event along this section (Figure 10). Although we do find streams having offset <6 m in Section S5 near Alashankou as mentioned in Hu et al. (2021), they are mostly located in an area with multiple fault splays. Thus, we suggest that the widespread ∼6–9 m displacements found along Sections S7–S4 in this study at sites where the fault has a single surface trace better represents the most recent surface rupture along the main fault. Along Section S2, we found consistent 6–9-m-high scarps that appear to result from a single rupture event. At the "Bear River" site, the fault strike is 300°, and the scarps of height 6.7–8.9 m are associated with lateral displacements of 11.6–15.7 m. The smallest lateral displacements found on Section S2 is close to the world's largest coseismic pure strike-slip offset as ∼15.5 m (Rodgers & Little, 2006), and considering the oblique slip component on S2, the total fault slip would be even higher. By assuming a slip-vector azimuth of 328°, these measurements yield slip of 14.7–19.9 m on a fault plane dipping 39°–55° to the south, based on a geometrical fault model presented in Figure 17). For Section S3, the

**Figure 12.** Pull-apart basin along the southern branch of Section S3 of the Dzhungarian Fault (see Figure 11a for location). (a) Orthorectified Pléiades imagery with scarps marked by yellow arrows. (b) Shaded-relief topography derived from Pléiades imagery, with the location (red star) of Sample DZH1 labeled. (c) and (d) Field photographs of the northern and the southern basin scarps (marked by yellow arrows; viewing perspective shown in "b"). (e) Field photo of where the infrared stimulated luminescence (IRSL) sample DZH1 was collected from loess at a depth of ∼65 cm below the terrace surface on the upthrown, southern, side of the fault (see "b"). The IRSL age is shown. (f) Drone-derived shaded-relief topography showing the five topographic profiles (B1–B5) labeled in blue. (g) Topographic profiles with their scarp heights (red text, in meters), diffusion ages (black text, in square meters), maximum scarp slopes (black text, in degrees), and fan slopes (gray text, in degrees).



19449194, 2022, 10, Downloaded from https://agupubs.onlinelibrary.wiley.com/doi/10.1029/2022TC007300 by Test, Wiley Online Library on [10/01/2023]. See the Terms and Conditions (https://onlinelibrary.wiley.com/terms-and-conditions) on Wiley Online Library for rules of use; OA articles are governed by the applicable Creative Commons License

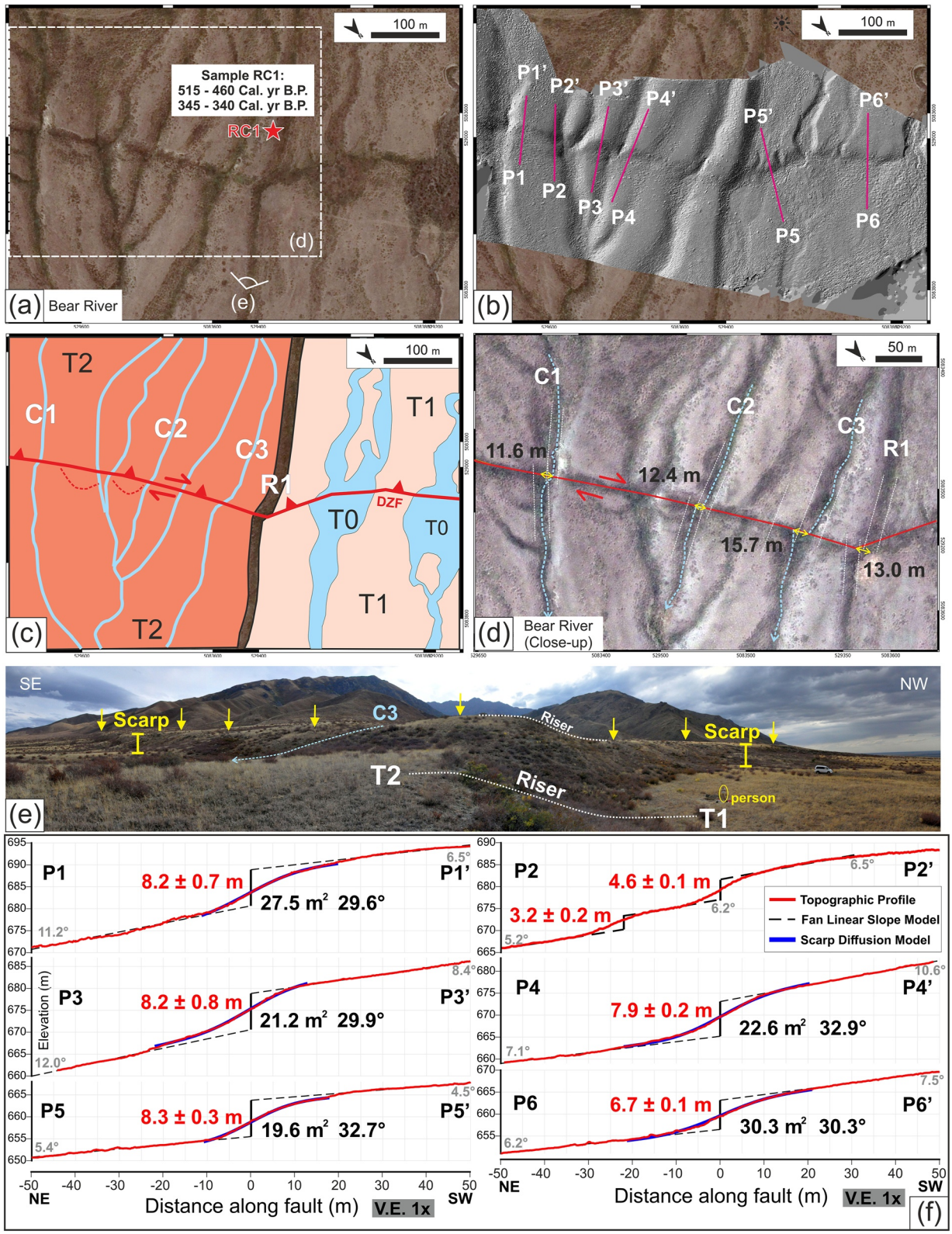


**Figure 13.**



19449194, 2022, 10, Downloaded from https://agupubs.onlinelibrary.wiley.com/doi/10.1029/2022TC007300 by Test, Wiley Online Library on [10/01/2023]. See the Terms and Conditions (https://onlinelibrary.wiley.com/terms-and-conditions) on Wiley Online Library for rules of use; OA articles are governed by the applicable Creative Commons License

19449194, 2022, 10, Downloaded from https://agupubs.onlinelibrary.wiley.com/doi/10.1029/2022TC007300 by Test, Wiley Online Library on [10/01/2023]. See the Terms and Conditions (https://onlinelibrary.wiley.com/terms-and-conditions) on Wiley Online Library for rules of use; OA articles are governed by the applicable Creative Commons License

complexity of faulting makes estimation of net slip more challenging, though minimum lateral displacements of 7.3–9.2 m were found along the main strike-slip segment. Assuming the fault dips 47° to the south, as having a similar dipping angle to Section S2, the average strike of 300°, and a slip-vector azimuth of 328°, we calculate a fault slip of 9.3–11.7 m, though note that this range is a minimum and does not take into account any slip on the numerous secondary faults within the region. We follow a similar approach to estimate the slip across the 6.9–10.2-m scarps on the splay fault at the Tentek River East site, in the transition zone between the Dzhungarian and the Lepsy Faults. This fault is parallel to the Lepsy Fault, with a trend of 280°. We estimate a fault slip of 10.4–15.4 m by assuming a slip-vector azimuth of 328° and a fault dip of 50°S, as was found for the adjacent Lepsy Fault (Campbell et al., 2015). These values imply a lateral slip of 5.2–7.7 m. A compilation of fault geometry and slip estimation of each section is in Table 3.

The continuity of scarps along the Dzhungarian Fault, their fresh morphology, and the large interpreted single-event offsets all point to an earthquake that ruptured most of the fault, from S7 in the south to S2 in the north, for a length of at least 250 km. Overall, the fault slip resulting from the most recent slip event on the Dzhungarian Fault appears to increase from the southeast to the northwest with the largest slip in the central Section S2, and possibly in S3 where we do not have constraints on single-event offset for both branches. This region of high slip is at the transition between NW-SE to almost W-E striking segments. It is also adjacent to a zone of splay faults branching westwards from the Dzhungarian Fault toward the Lepsy Faults. Although there is no direct linkage of rupture between the Dzhungarian and Lepsy Faults, the widely distributed Holocene faults between them are each separated by no more than 3 km, raising the possibility that the two main faults ruptured simultaneously during a single earthquake, which would have a rupture length of at least 375 km (RS1 in Table 3).

Relatively complex multifault rupture patterns have been observed in a number of recent events in which slip has occurred on several splays or branched fault systems, such as in the 1992 Landers earthquake (Sieh et al., 1993), the 2010 Darfield earthquake (Quigley et al., 2019), and the 2016 Kaikoura earthquake (Hollingsworth et al., 2017). In this last example, large (>10 m) multifault ruptures with displacement changing from strike-slip to thrust motion along strike were observed (Hollingsworth et al., 2017; Xu et al., 2018), which is similar to the scenario we have presented here. We note that scenarios with shorter rupture lengths cannot be discounted, and we also consider a scenario in which the Dzhungarian Fault ruptured alone during its latest earthquake from Sections S7 to S2, with a rupture length of 248 km (RS2 in Table 3).

### 6.2. Earthquake Chronology

We have relatively limited constraints on the timing of the most recent event on the Dzhungarian and Lepsy Faults. The most detailed paleoseismic information so far comes from Hu et al. (2021), who recognize four events from a trench along S7 (Figure 8b), with the most recent rupture after 6.6 ka, a penultimate event in the range 12.2–6.6 ka, a third in the range 19.4–17.3 ka, and a fourth either prior to ∼19.4 ka, or occupying the same 19.4–17.3 ka range as the following event. Hu et al. (2021) provide an average recurrence time of ∼4–6 ka. From our fieldwork, we have a single IRSL sample DZH1 from a displaced terrace along S3 that is dated to 12 ka which must predate the most recent event (Figure 12). At the primary and secondary scarps at the Bear River site (Section S2), two radiocarbon samples (RC1 and RC2) from the displaced terraces yield ages of ∼400 and ∼4,000 Cal. yr B.P., respectively (Figures 13 and 14). We note that both our snail samples for radiocarbon dating might not represent the terrace abandoned ages since it is likely that they dug into the gravel layer a long time after gravel deposition although snail ages do show consistency with terrace deposition age in other region (e.g., Stahl et al., 2022). Though limited, our age results may be compatible with those of Hu et al. (2021), if we assume that the older (∼4,000 Cal. yr B.P.) rather than younger (∼400 Cal. yr B.P.) age from the Bear River site is more representative of terrace deposition age. In that case, our age data support a single large earthquake rupture along

**Figure 13.** (a) Orthorectified Pléiades imagery showing fault scarp and offset channels at the Bear River site (81.37°E, 45.90°N) within Section S2 of the Dzhungarian Fault (see "Figure 7b" or "Figure 14a" for location). The location (red star) and age of Sample RC1 are annotated. (b) Drone-derived shaded-relief digital elevation model (DEM) showing the same view as in "a." Locations of topographic profiles are shown. (c) Geomorphic map showing the extents of two terraces (T1 and T2) and the riser (R1) between them. (T0 is the current river channel.) (d) Close-up Pléiades image showing the three offset channels (C1, C2, and C3) and the terrace riser (R1) with amounts of dextral offsets annotated in meters. (e) Panoramic field photograph showing the scarp, which is of similar height in both terraces T1 and T2. See "a" for viewing perspective. (f) The six topographic profiles (P1–P6) extracted from drone DEMs showing scarp heights (red text, in meters), diffusion ages (black text, in square meters), maximum scarp slopes (black text, in degrees), and fan slopes (gray text, in degrees).

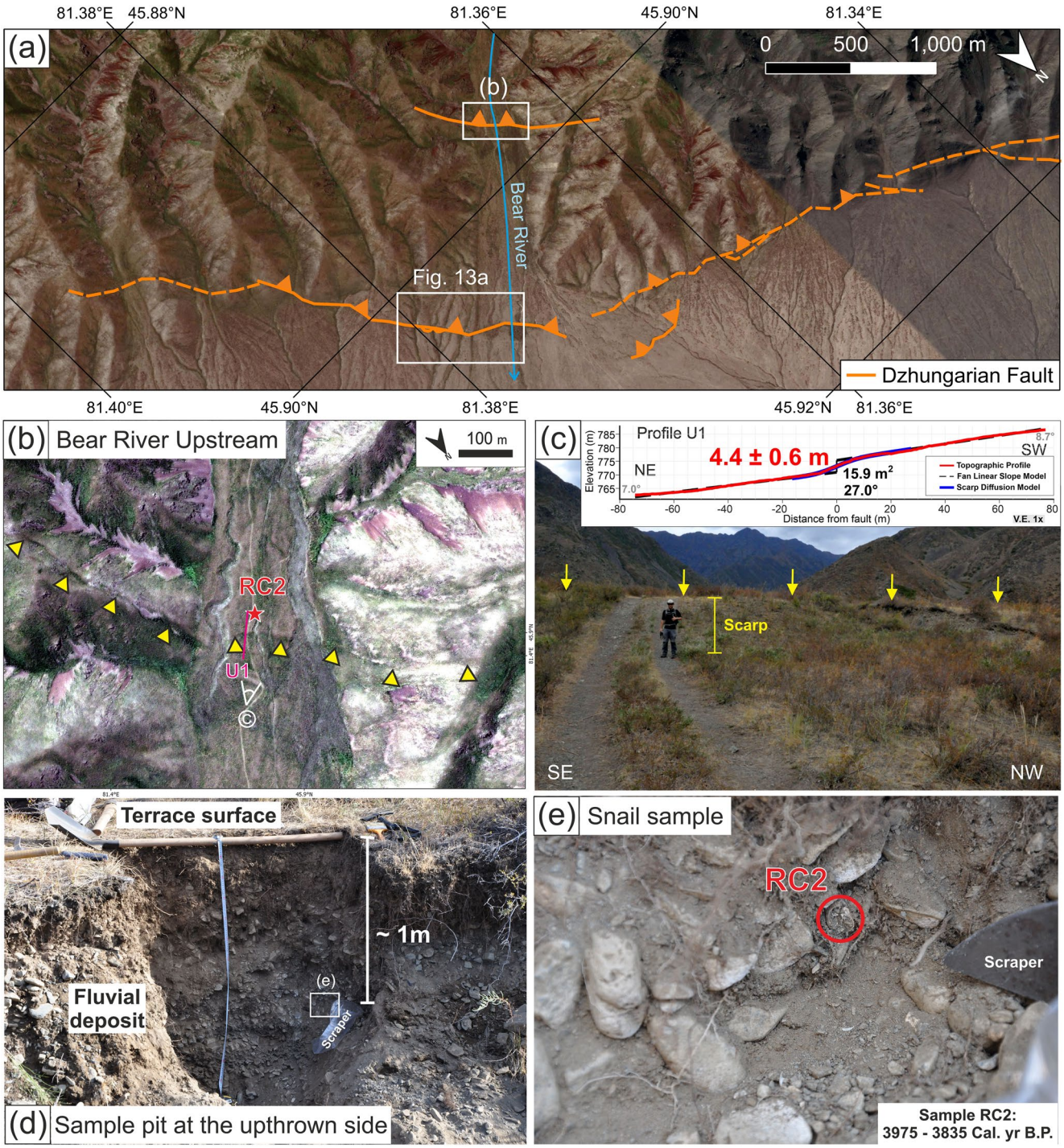


**Figure 14.** (a) Orthorectified Pléiades imagery showing the second scarp (yellow arrows) upstream from the Bear River site (81.36°E, 45.90°N). The locations of sample RC2 (red star) and the differential GPS (dGPS) profile (short red line) are marked. (b) Field photo of the scarp with the dGPS topographic profile and morphological scarp dating results shown as an inset. (c and d) Field photographs of the sample pit and the gastropod sample RC2 (red circle) along with its calibrated radiocarbon age.

the Dzhungarian Fault, occurring within the last ~4 ka. It is possible that this is the only earthquake to have occurred in the last ~17 ka, if we consider the scarps along the pull-apart basin in S3 shown in Figure 12 to result from a single event, as implied by the absence of beveling at the top of the scarp. One profile at that site showed a lower amount of slip that, if real, would mean that more than one earthquake has occurred within the last 17 ka.



19449194, 2022, 10, Downloaded from https://agupubs.onlinelibrary.wiley.com/doi/10.1029/2022TC007300 by Test, Wiley Online Library on [10/01/2023]. See the Terms and Conditions (https://onlinelibrary.wiley.com/terms-and-conditions) on Wiley Online Library for rules of use; OA articles are governed by the applicable Creative Commons License

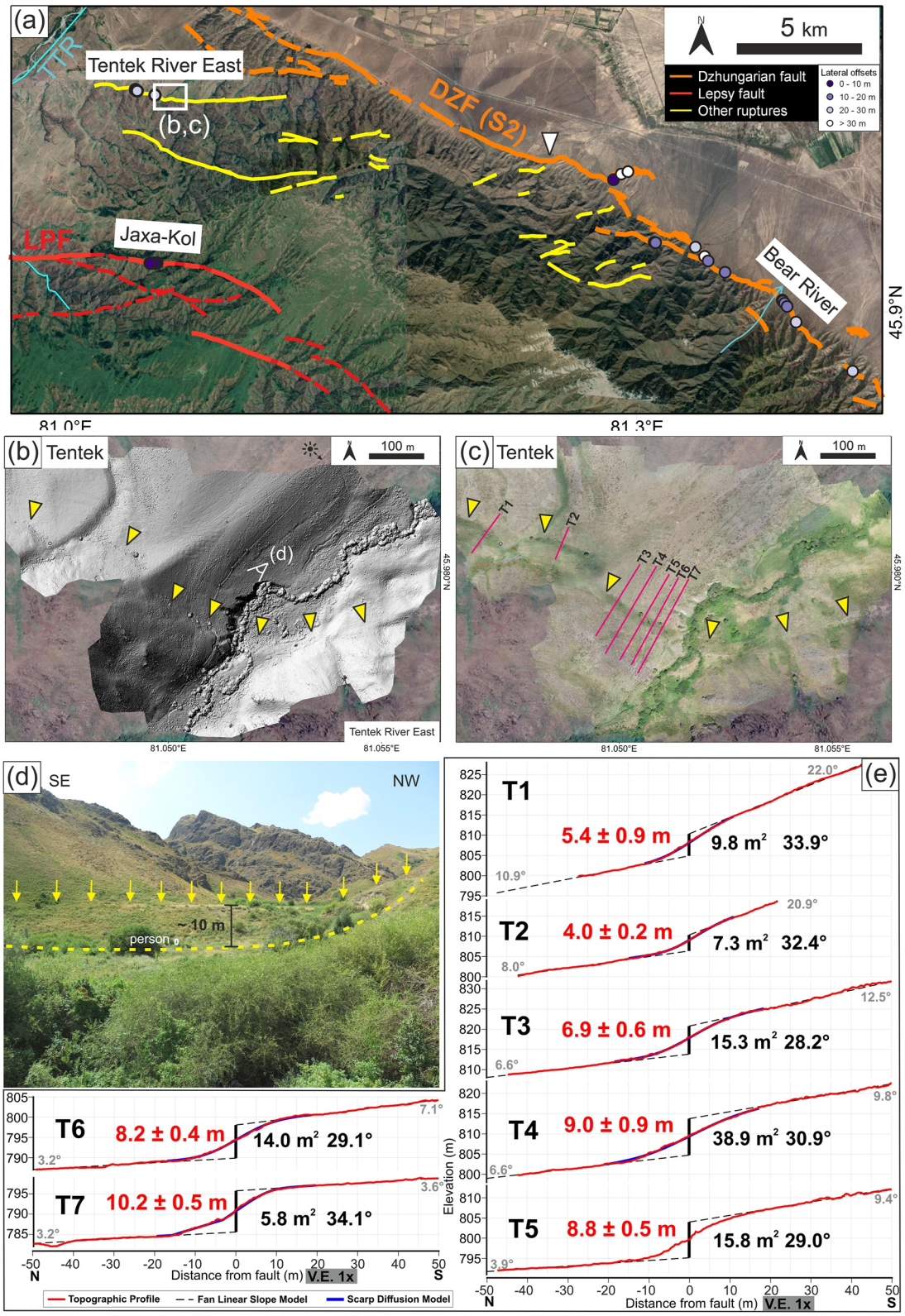


**Figure 15.** (a) Bing Map imagery showing the transition area between the Lepsy and Dzhungarian Faults. The white triangle marks the transition where the heights of the S2 fresh scarps drop from 6–9 to <5 m. (b and c) Drone-derived shaded-relief topography and orthorectified imagery showing the fresh scarps (marked by yellow arrows) and the locations of the seven topographic profiles (T1–T7) at the Tentek River (TTR) East site (81.05°E, 46.00°N). (d) Field photograph of the scarp, marked by yellow arrows on top and a dashed line at the bottom (see "b" for viewing perspective). (e) The seven profiles T1–T7 with their morphological scarp dating results.



19449194, 2022, 10, Downloaded from https://agupubs.onlinelibrary.wiley.com/doi/10.1029/2022TC007300 by Test, Wiley Online Library on [10/01/2023]. See the Terms and Conditions (https://onlinelibrary.wiley.com/terms-and-conditions) on Wiley Online Library for rules of use; OA articles are governed by the applicable Creative Commons License

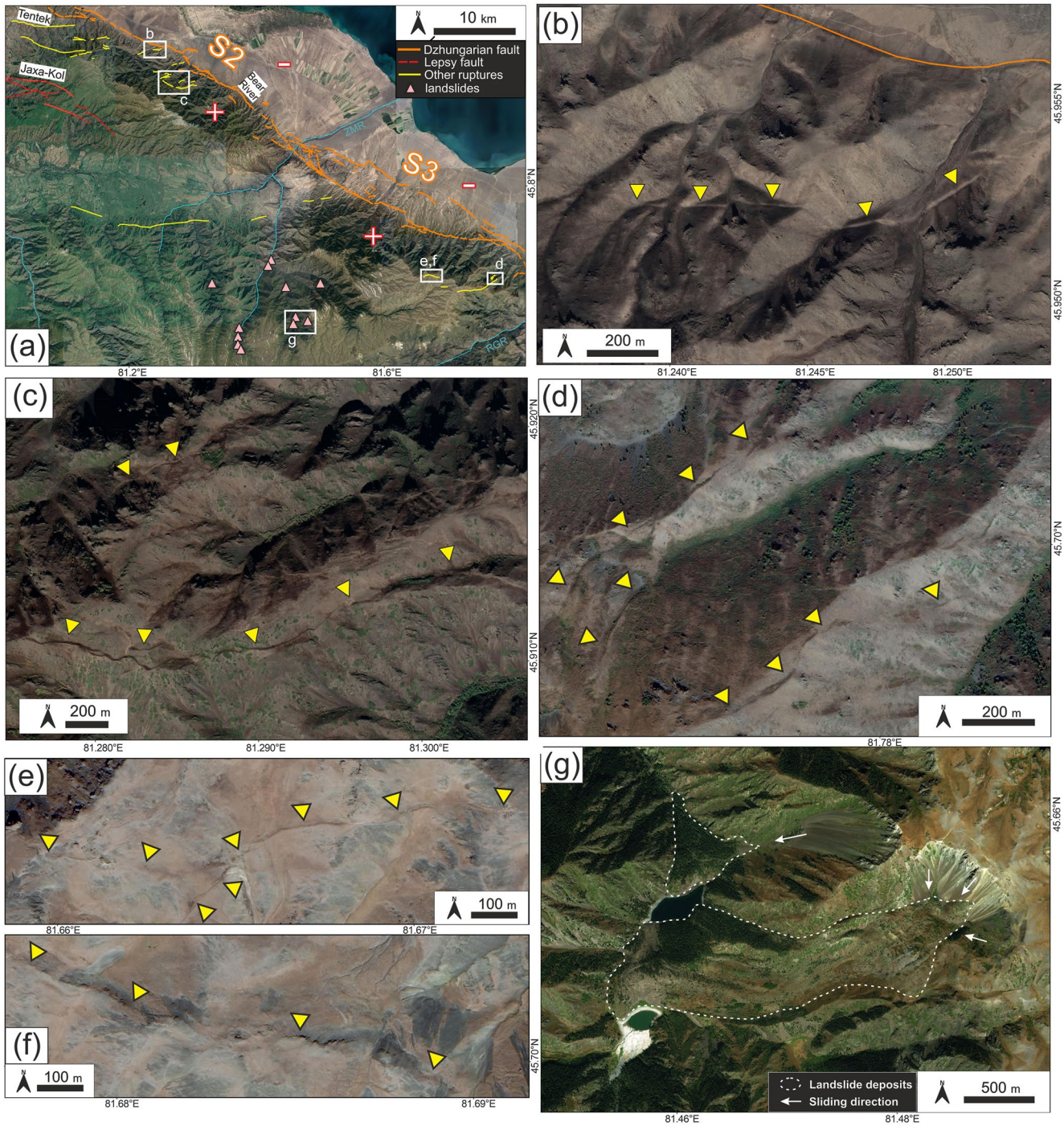


**Figure 16.** (a) Bing Map imagery showing the northern Dzhungarian Alatau with locations of mapped fault traces, other ruptures, and landslides. (b–f) Google Earth imagery showing fresh fractures (marked by yellow arrows) on the hill surfaces close to S2 (near 81.29°E, 45.92°N) and S3 (near 81.77°E, 45.70°N). (g) Bing Map imagery showing examples of large bedrock landslides (at 81.47°E, 45.65°N).

Campbell et al. (2015) infer a large surface-rupturing earthquake along the Lepsy Fault within the last 400 years, which they tentatively assign to an earthquake in 1716 described in Mushketov and Orlov's catalog (1893). The evidence for this <400-year age comes from one location (Ayak-Kol). Our morphological dating, however, suggests that the scarps at Ayak-Kol might be substantially older, in the range 5.3–3.5 ka. At several sites, Campbell et al. (2015) find evidence for deformation within that older range: ponded sediments near Jaxa-Kol date to at least 2,000 years ago, 5,000-year-old fluvial sediments are uplifted by the scarp at the Shynzhyly River,



19449194, 2022, 10, Downloaded from https://agupubs.onlinelibrary.wiley.com/doi/10.1029/2022TC007300 by Test, Wiley Online Library on [10/01/2023]. See the Terms and Conditions (https://onlinelibrary.wiley.com/terms-and-conditions) on Wiley Online Library for rules of use; OA articles are governed by the applicable Creative Commons License

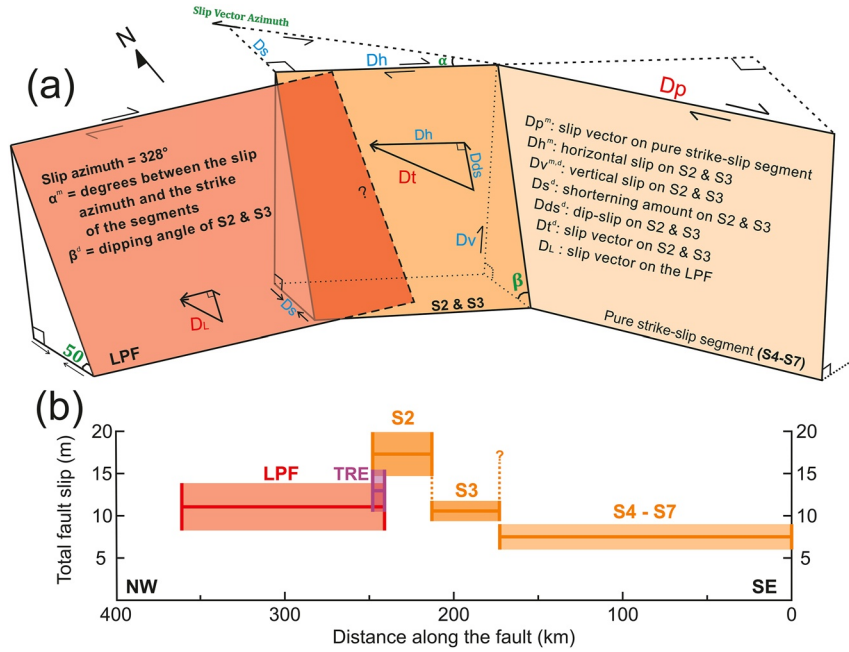


**Figure 17.** (a) Sketch showing the simplified fault geometry including the Lepsy Fault (LPF) and Sections S2–S7 of the Dzhungarian Fault. The slip on Sections S2 and S3, which includes substantial vertical as well as horizontal components of slip, are estimated assuming a constant slip-vector azimuth of 328° for all the segments. The superscript "m" and "d" mean the "measured" and "derived" components, respectively. Note that the vertical slip was measured on S2 but was derived on S3. Note that slip-vector azimuth ($D_L$) for the LPF has been determined independently based on the interpretations by Campbell et al. (2015) and is consistent with the assumed value used here. (b) Total fault slip interpreted as being from the most recent event on different segments in this multifault system, including Dzhungarian Fault (orange), Lepsy (red), and the Tentek River East scarps (TRE; purple).

and soft-sediment deformation at Ayak-Kol has affected sediments dated at 5,328–4,931 calibrated radiocarbon years B.P. In summary, the available age data indicates a rupture on the Lepsy Fault within the last ~5,000 years, but suggests the <400-year constraint previously interpreted from Ayak-Kol is too young. Further investigation may confirm whether the young ages at Ayak-Kol are erroneous, or whether the scarp profiles appear anomalously old.

**Table 3**
*The Two Rupture Scenarios Proposed in This Study*

| Sections | Length (km) | Strike | Dip | Measured minimum lateral slip (m) | Measured minimum vertical slip (m) | Inferred average slip (AD) (m) |
|---|---|---|---|---|---|---|
| LPF | 120[a] | 290°[a] | 50°S[a] | 5–9[a] | 5–9[a] | 8.2–13.8[a] |
| TRE | 7 | 280° | 50°S | - | 6.9–10.2 | 10.4–15.4 |
| S2 | 35 | 300° | 39°–55°S | 11.6–15.7 | 6.7–8.9 | 14.7–19.9 |
| S3 | 40 | 300° | 47°S | 7.3–9.2 | - | 9.3–11.7 |
| S4-S7 | 173 | 328° | 90° | 8.8 | - | 8.8 |

| Scenarios | Rupture sections | SRL[b] (km) | AD (m) | $M_w$ from AD[c] | $M_w$ from SRL[d] | $M_w$ from seismic moment | Slip-to-length ratio |
|---|---|---|---|---|---|---|---|
| RS1 | LPF + TRE + (S2–S7) | 375 | 8.2–19.9 | 7.9–8.2 | 8.1 | 8.1–8.4 | $2.6 \times 10^{-5}$–$3.7 \times 10^{-5}$ |
| RS2 | S2–S7 | 248 | 8.8–19.9 | 7.9–8.2 | 7.8 | 7.9–8.2 | $4.0 \times 10^{-5}$–$5.5 \times 10^{-5}$ |

*Note*. TRE, Tentek River East.

[a]The parameters of the Lepsy Fault (LPF) are all from Campbell et al. (2015). [b]SRL, Surface Rupture Length. [c]$M_w$ is calculated from $M_w = 7.04 + 0.89\log(AD)$ in Wells and Coppersmith (1994). [d]$M_w$ is calculated from $\log(SRL) = -2.943 + 0.681\ M_w$ in Thinbaijam et al. (2017).



19449194, 2022, 10, Downloaded from https://agupubs.onlinelibrary.wiley.com/doi/10.1029/2022TC007300 by Test, Wiley Online Library on [10/01/2023]. See the Terms and Conditions (https://onlinelibrary.wiley.com/terms-and-conditions) on Wiley Online Library for rules of use; OA articles are governed by the applicable Creative Commons License

19449194, 2022, 10, Downloaded from https://agupubs.onlinelibrary.wiley.com/doi/10.1029/2022TC007300 by Test, Wiley Online Library on [10/01/2023]. See the Terms and Conditions (https://onlinelibrary.wiley.com/terms-and-conditions) on Wiley Online Library for rules of use; OA articles are governed by the applicable Creative Commons License

In summary, the majority of available evidence is consistent with a single rupture along the Dzhungarian and Lepsy Faults that displaced terraces that are as little as 4,000 years in age, and which has caused ponding against the scarps for at least 2,000 years. A later earthquake within the last 400 years may have occurred along the Lepsy Fault, as suggested by dating at Ayak-Kol, but morphological scarp dating at all of our sites, including those along the Lepsy Fault, are 10–24 $m^2$ in average (Figures S2–S5 in Supporting Information S1), indicating an onset of scarp degradation in the range 6–2 ka.

Our COPD analysis for Sections S4 and S5 of the Dzhungarian Fault yielded peaks in lateral offset at 8.8 m, 15.2, and 23.7 m, which we inferred to represent slip in the last three earthquakes, with amounts of 8.8 m, 6.4, and 8.5 m, respectively. Hu et al. (2021) interpret three or four earthquakes to have occurred in the southern Dzhungarian Fault over the last 19.4–17.3 ka with an average recurrence interval of 4–6 ka. Further investigations may determine whether the most recent event was closer to 4,000 or 2,000 years ago. If the last three earthquakes have accrued an average slip of 23.7 m, and if those earthquakes have occurred within the last 19.4–17.3 ka with an average recurrence interval of 4–6 ka, the inferred lateral slip rate would be 1.2–1.4 mm/yr and the age of 25.7 ± 5.8 ka for ∼50 m of offset measured by Campbell et al. (2013) is plausible.

### 6.3. Earthquake Magnitudes and Scaling

We consider the likely magnitudes in two paleo-earthquake scenarios. Rupture Scenario 1 (RS1) assumes the Lepsy Fault, Dzhungarian Fault, and the faults within the transition zone between them ruptured together in a single event. In Rupture Scenario 2 (RS2) only Sections S2–S7 of the Dzhungarian Fault ruptured together. We first use the empirical relationships in Wells and Coppersmith (1994) and Thingbaijam et al. (2017). By using the mean coefficients for strike-slip faulting from the average slip (AD), which is the range of AD on each ruptured sections, we calculate moment-magnitudes of $M_w$ 7.9–8.2 for both scenarios (Table 3). Applying the scaling relationship between magnitude and surface rupture length (SRL) yields $M_w$ 8.1 for RS1 and $M_w$ 7.8 for RS2. We also calculate the magnitudes based on the combining seismic moment ($M_o$) released from each rupture segment

$$M_w = \frac{2}{3}\log M_o - 6.06, \text{ where } M_o = \mu \text{AD}$$

where $\mu$ is the shear modulus $3 \times 10^{10}$ $Nm^2$, $D$ is the average slip and $A$ is the rupture area on the fault plane (Aki, 1966; Kanamori, 1977). We assume the depth is 15–30 km given typical earthquake depths within the Tien Shan, though we note that event depths down to ∼40 km have been modeled in the adjacent Kazakh steppe (Alinaghi & Krüger, 2014; Sloan et al., 2011; Figure 1a). Applying the range of depths and the other source parameters listed in Table 3 yields the moment magnitudes in the range of $M_w$ 8.1–8.4 for the combined Lepsy and Dzhungarian Faults (RS1), and $M_w$ 7.9–8.2 for the Dzhungarian Fault alone (RS2). The ranges of the estimated moment magnitudes are similar to magnitudes found for the 1889 Chilik ($M_w$ 8.0–8.3), and the 1911 Chon-Kemin ($M_w$ 7.8–8.0) earthquakes (Abdrakhmatov et al., 2016; Arrowsmith et al., 2017; Krüger et al., 2017; Kulikova & Krüger, 2015), which suggests the northern Tien Shan could have similarly large magnitude earthquakes as the central Tien Shan despite the slower strain rate in the north.

We calculate the ranges of the slip-to-length ratios for each scenario from the average minimum slip and the average maximum slip among each ruptured segment and then divided by the total rupture length. Rupture of the Dzhungarian Fault alone yields a ratio of $4.0 \times 10^{-5}$–$5.5 \times 10^{-5}$, the combined Lepsy-Dzungarian rupture yields a ratio of $2.6 \times 10^{-5}$–$3.7 \times 10^{-5}$ (Table 3). These ratios are generally compatible with global scaling relationships which are in the range of 1–$10 \times 10^{-5}$ (Scholz, 1986; Wells & Coppersmith, 1994; Wesnousky, 2008; Figure 2). That the Dzhungarian Fault is inferred to follow global scaling relationships between slip and length, even though it is within an intracontinental and relatively slowly deforming setting, might be due to the structural maturity of the Dzhungarian Fault since it is a reactivated fault that has formed since the Paleozoic (Campbell et al., 2015; Manighetti et al., 2007; Voytovich, 1965).

Comparing the two rupture scenarios with renowned great intraplate earthquakes that have well-studied surface ruptures, the combined Dzhungarian-Lepsy rupture length is similar to those in the 1905 Bulnay (375 km) and the 1957 Gobi-Altay (360 km) earthquakes (Kurtz et al., 2018; Rizza et al., 2015) but fault slip in the Dzhungarian-Lepsy rupture is larger (Figure 2). Adding our findings of prehistorical ruptures along the Dzhungarian Alatau to the other examples of giant intraplate earthquake ruptures, we find them roughly in line with the

19449194, 2022, 10, Downloaded from https://agupubs.onlinelibrary.wiley.com/doi/10.1029/2022TC007300 by Test, Wiley Online Library on [10/01/2023]. See the Terms and Conditions (https://onlinelibrary.wiley.com/terms-and-conditions) on Wiley Online Library for rules of use; OA articles are governed by the applicable Creative Commons License

global scaling relationships and do not find much discrepancy with plate-boundary earthquakes (Figure 2). There are several high stress drop events, meaning more energy is released for a given-magnitude earthquake, such as the Bhuj and the Assam earthquakes as having large slip and rupture area (Bilham & England, 2001; Copley et al., 2011; Negishi et al., 2002). Some studies also stated stress drops for intraplate earthquakes tend to be higher than for interplate ones (Allmann & Shearer, 2009; Kanamori & Anderson, 1975); however, the compilation of great earthquakes in the Tien Shan and Mongolia in this study and some stable continental earthquake examples in Yang et al. (2021) seem to disagree with this idea. We suggest the various settings for intraplate faults such as their maturity, local lithology, crustal thickness, and slip heterogeneity might cause variability in stress drop and slip-to length ratio (Thingbaijam et al., 2017 and the references therein). Therefore, whether intracontinental faults do have particular rupture behaviors and how different they are from faults in plate-boundary settings still require further investigation.

### 6.4. Implications for Intraplate Earthquakes and Faulting in the Tien Shan Region

It is worth noting that the latest rupture does not propagate along the general strike of the Dzhungarian Fault into Sections S1 and S0 but instead goes along the Lepsy Fault whose strike is misoriented to the inferred slip vector of ~328°. It is possible that multifault ruptures start at the Lepsy Fault and further trigger movement along the central to SE Dzhungarian Fault, which might explain the absence of fresh ruptures in the northern Dzhungarian Fault and the additional fault splays between the Lepsy and Dzhungarian Faults adjacent to the central part of the Dzhungarian Fault (S2 and S3). Several cases globally (e.g., the 2010 El Mayor-Cucapah and the 2010 Darfield earthquakes) have shown that misoriented faults can trigger cascading ruptures across the fault network (Fletcher et al., 2016; Quigley et al., 2019), which might also be the case for the combined Dzhungarian-Lepsy rupture. Moreover, the increasing component of shortening from the southern part of the Dzhungarian Fault to the Lepsy Fault is consistent with the regional pattern of deformation in the Dzhungarian Alatau and wider Tien Shan region (Figure 1b) (Abdrakhmatov et al., 1996; Zubovich et al., 2010) and the misoriented segments like the Lepsy Fault might be the primary structures for the mountain building process in this region as they have a similar trend to the E-W oriented ridges of the Dzhungarian Alatau. Our data imply that a major boundary faults in the region could have a joint rupture with shorter local structures, which is still likely to trigger larger-magnitude earthquakes than expected for single-fault ruptures.

## 7. Conclusions

Our results provide a valuable example of a paleo-earthquake which ruptured a major intracontinental strike-slip fault. Our observations and analysis of the paleo-earthquake ruptures from satellite imagery and field surveys indicate that a great earthquake likely occurred in the last 4,000 years on the Dzhungarian Fault, with a rupture length of up to 375 km for a combined Dzhungarian-Lepsy rupture. We interpret this complex earthquake to have involved slip on two separate faults and distributed faulting in between. The total fault slip is up to ~20 m on the northern oblique-slip sections and 6–9 m on the southern pure strike-slip section. Our estimated paleo-earthquake magnitudes for a combined rupture of the Dzhungarian and Lepsy Faults reach up to $M_w$ 8.4, which would place it amongst the largest known intracontinental earthquakes. Despite these particularly large parameters, this paleo-earthquake is consistent with the global scaling relationships between slip and length, as are other large intracontinental earthquakes in Tien Shan and Mongolia. We show that the Lepsy Fault may not have a high slip-to-length ratio as previously suggested and we demonstrate the importance of meticulous fault mapping for estimation of accurate scaling relationships. More examples from either historical or prehistorical earthquakes would be helpful to further analyze and summarize fault behaviors within intracontinental settings.

## Data Availability Statement

Commercial Pléiades satellite data used within this analysis were obtained under academic license from Airbus and are available for purchase (https://www.intelligence-airbusds.com/imagery/constellation/pleiades/). Point clouds of all digital elevation data used in this study are archived and available through OpenTopography in five data sets titled as "Survey of the Tentek River, Dzhungarian Fault, Kazakhstan, July 2019" (https://doi.org/10.5069/G9KK9906), "Survey of the pull-apart basin, Dzhungarian Fault, Kazakhstan, July 2019" (https://doi.org/10.5069/G9FT8J8G), "Survey of the Rygayty River, the Dzhungarian Fault, Kazakhstan, July 2019"

(https://doi.org/10.5069/G9B27SHM), "Dzhungarian Fault slip rate site "Bear River": Kazakhstan, 2015" (https://doi.org/10.5069/G91834PR), and "Point clouds derived from satellite imagery, Dzhungarian Fault" (https://doi.org/10.5069/G9XS5SMQ). Any use of trade, firm, or product names is for descriptive purposes only and does not imply endorsement by the U.S. Government.

**Acknowledgments**
This work was supported by the Natural Environment Research Council (NERC)-Economic and Social Research Council (ESRC) Increasing Resilience to Natural Hazards program "Earthquakes without Frontiers" (NE/J02001X/1), by the NERC-funded the Centre for the Observation and Modelling of Earthquakes, Volcanoes and Tectonics (COMET) (GA/13/M/031), by the North Atlantic Treaty Organization (NATO) Science for Peace and Security Multi-Year program "Environmental security in Kazakhstan and Kyrgyzstan" (G5690), and by the Leverhulme Trust Research Project Grant "EROICA" (RPG-2018-371). Fieldwork in 2019 was supported by the Vladimir Potanin Research Fund for Earth Sciences at St. Edmund Hall, Oxford. J. R. Elliott was supported by a Royal Society University Research fellowship (UF150282). Satellite imagery was provided through the funding from COMET. We thank Tamarah King, Stéphane Baize, Suzanne Hecker, and one anonymous reviewer for the helpful comments on the manuscript.

## References

Abdrakhmatov, K. E., Aldazhanov, S. A., Hager, B. H., Hamburger, M. W., Herring, T. A., Kalabaev, K. B., et al. (1996). Relatively recent construction of the Tien Shan inferred from GPS measurements of present-day crustal deformation rates. *Nature*, *384*(6608), 450–453. https://doi.org/10.1038/384450a0

Abdrakhmatov, K. E., Djanuzakov, K. D., & Delvaux, D. (2002). Active tectonics and seismic hazard of the Issyk-Kul Basin in the Kyrgyz Tian-Shan. In J. Klerkx, & B. Imanackunov (Eds.), *Lake Issyk-Kul: Its natural environment* (pp. 147–160). Netherlands: Springer. https://doi.org/10.1007/978-94-010-0491-6_11

Abdrakhmatov, K. E., Walker, R. T., Campbell, G. E., Carr, A. S., Elliott, A. J., Hilleman, C., et al. (2016). Multisegment rupture in the 11 July 1889 Chilik earthquake (Mw 8.0-8.3), Kazakh Tien Shan, interpreted from remote sensing, field survey, and paleoseismic trenching. *Journal of Geophysical Research: Solid Earth*, *121*, 4615–4640. https://doi.org/10.1002/2015JB012763

Abdrakhmatov, K. E., Weldon, R. J., Thompson, S. C., Burbank, D. W., Ch, R., Miller, M., & Molnar, P. (2001). Origin, direction, and rate of modern compression of the central Tien Shan (Kyrgyzstan). *Russian Geology and Geophysics*, *42*(10), 1585–1609.

Ainscoe, E. A., Abdrakhmatov, K. E., Baikulov, S., Carr, A. S., Elliott, A. J., Grützner, C., & Walker, R. T. (2019). Variability in surface rupture between successive earthquakes on the Suusamyr Fault, Kyrgyz Tien Shan: Implications for palaeoseismology. *Geophysical Journal International*, *216*(1), 703–725. https://doi.org/10.1093/gji/ggy457

Aki, K. (1966). Generation and propagation of G waves from the Niigata Earthquake of June 16, 1964: Part 2. Estimation of earthquake moment, released energy, and stress-strain drop from the G wave spectrum. In *Bulletin of the Earthquake Research Institute, University of Tokyo* (Vol. 44(1), pp. 73–88). The Earthquake Research Institute, University of Tokyo. https://ci.nii.ac.jp/naid/120000871042/en/

Alinaghi, A., & Krüger, F. (2014). Seismic array analysis and redetermination of depths of earthquakes in Tien-Shan: Implications for strength of the crust and lithosphere. *Geophysical Journal International*, *198*(2), 1111–1129. https://doi.org/10.1093/gji/ggu141

Allmann, B. P., & Shearer, P. M. (2009). Global variations of stress drop for moderate to large earthquakes. *Journal of Geophysical Research*, *114*, B01310. https://doi.org/10.1029/2008JB005821

Amey, R. M. J., Elliott, J. R., Hussain, E., Walker, R. T., Pagani, M., Silva, V., et al. (2021). Significant seismic risk potential from buried faults beneath Almaty City, Kazakhstan, revealed from high-resolution satellite DEMs. *Earth and Space Science*, *8*(9), 1–25. https://doi.org/10.1029/2021EA001664

Arrowsmith, J. R., Crosby, C. J., Korzhenkov, A. M., Mamyrov, E., Povolotskaya, I., Guralnik, B., & Landgraf, A. (2017). Surface rupture of the 1911 Kebin (Chon-Kemin) earthquake, Northern Tien Shan, Kyrgyzstan. *Geological Society, London, Special Publications*, *432*(1), 233–253. https://doi.org/10.1144/SP432.10

Avouac, J.-P., Ayoub, F., Wei, S., Ampuero, J. P., Meng, L., Leprince, S., et al. (2014). The 2013, Mw 7.7 Balochistan earthquake, energetic strike-slip reactivation of a thrust fault. *Earth and Planetary Science Letters*, *391*, 128–134. https://doi.org/10.1016/j.epsl.2014.01.036

Avouac, J.-P., Tapponnier, P., Bai, M., You, H., & Wang, G. (1993). Active faulting and folding along the northern Tien Shan and Late Cenozoic rotation of the Tarim relative to Dzungaria and Kazakhstan. *Journal of Geophysical Research*, *98*(B4), 6755–6804. https://doi.org/10.1029/92JB01963

Baize, S., Reicherter, K., Avagyan, A., Belyashov, A., Pestov, E., Vittori, E., et al. (2019). First assessment of recent tectonics and paleoearthquakes along the Irtysh fault (eastern Kazakhstan). *Geomorphology*, *326*, 90–106. https://doi.org/10.1016/j.geomorph.2018.09.013

Bi, H., Zheng, W., Lei, Q., Zeng, J., Zhang, P., & Chen, G. (2020). Surface slip distribution along the West Helanshan Fault, Northern China, and its implications for fault behavior. *Journal of Geophysical Research: Solid Earth*, *125*, e2020JB019983. https://doi.org/10.1029/2020JB019983

Bilham, R., & England, P. (2001). Plateau 'pop-up' in the great 1897 Assam earthquake. *Nature*, *410*(6830), 806–809. https://doi.org/10.1038/35071057

Bindi, D., Parolai, S., Gómez-Capera, A., Locati, M., Kalmeteva, Z. A., & Mikhailova, N. (2014). Locations and magnitudes of earthquakes in Central Asia from seismic intensity data. *Journal of Seismology*, *18*(1), 1–21. https://doi.org/10.1007/s10950-013-9392-1

Bogdanovich, K. I., Kark, I. M., Korolkov, B. Y., & Mushketov, D. I. (1914). *Earthquake in northern District of Tien Shan, 22 December 1910 (in Russian)*. St Petersburg, Russia: Communications of the Geological Community.

Bollinger, L., Klinger, Y., Forman, S., Chimed, O., Bayasgalan, A., Munkhuu, U., et al. (2021). 25,000 Years long seismic cycle in a slow deforming continental region of Mongolia. *Scientific Reports*, *11*, 17855. https://doi.org/10.21203/rs.3.rs-310793/v1

Burchfiel, B. C., Brown, E. T., Deng, Q., Feng, X., Li, J., Molnar, P., et al. (1999). Crustal shortening on the margins of the Tien Shan, Xinjiang, China. *International Geology Review*, *41*(8), 665–700. https://doi.org/10.1080/00206819909465164

Burtman, V. (1975). Structural geology of Variscan Tien Shan, USSR. *American Journal of Science*, *275*, 157–186.

Burtman, V. (2008). Nappes of the southern Tien Shan. *Russian Journal of Earth Sciences*, *10*(1), ES1006. https://doi.org/10.2205/2007es000223

Campbell, G. E., Walker, R. T., Abdrakhmatov, K. E., Carolin, S., Carr, A. S., Elliott, J. R., et al. (2019). Rapid late Quaternary slip, repeated prehistoric earthquake rupture, and widespread landsliding associated with the Karakudzhur Thrust, Central Kyrgyz Tien Shan. *Tectonics*, *38*, 3740–3764. https://doi.org/10.1029/2018TC005433

Campbell, G. E., Walker, R. T., Abdrakhmatov, K. E., Jackson, J. A., Elliott, J. R., Mackenzie, D., et al. (2015). Great earthquakes in low strain rate continental interiors: An example from SE Kazakhstan. *Journal of Geophysical Research: Solid Earth*, *120*, 5507–5534. https://doi.org/10.1002/2015JB011925

Campbell, G. E., Walker, R. T., Abdrakhmatov, K. E., Schwenninger, J., Jackson, J. A., Elliott, J. R., & Copley, A. (2013). The Dzhungarian Fault: Late Quaternary tectonics and slip rate of a major right-lateral strike-slip fault in the northern Tien Shan region. *Journal of Geophysical Research: Solid Earth*, *118*, 5681–5698. https://doi.org/10.1002/jgrb.50367

Carson, M. A., & Kirkby, M. J. (1972). *Hillslope form and process* (3rd ed.). Cambridge University Press.

Catherine, J. K., Gahalaut, V. K., & Sahu, V. K. (2005). Constraints on rupture of the December 26, 2004, Sumatra earthquake from far-field GPS observations. *Earth and Planetary Science Letters*, *237*(3), 673–679. https://doi.org/10.1016/j.epsl.2005.07.012

Chen, W.-P., & Molnar, P. (1983). Focal depths of intracontinental and intraplate earthquakes and their implications for the thermal and mechanical properties of the lithosphere. *Journal of Geophysical Research*, *88*(B5), 4183–4214. https://doi.org/10.1029/JB088iB05p04183



19449194, 2022, 10, Downloaded from https://agupubs.onlinelibrary.wiley.com/doi/10.1029/2022TC007300 by Test, Wiley Online Library on [10/01/2023]. See the Terms and Conditions (https://onlinelibrary.wiley.com/terms-and-conditions) on Wiley Online Library for rules of use; OA articles are governed by the applicable Creative Commons License

Colman, S. M., & Watson, K. E. N. (1983). Ages estimated from a diffusion equation model for scarp degradation. *Science*, *221*(4607), 263–265. https://doi.org/10.1126/science.221.4607.263

Copley, A., Avouac, J.-P., Hollingsworth, J., & Leprince, S. (2011). The 2001 Mw 7.6 Bhuj earthquake, low fault friction, and the crustal support of plate driving forces in India. *Journal of Geophysical Research*, *116*. B08405. https://doi.org/10.1029/2010JB008137

Cording, A., Hetzel, R., Kober, M., & Kley, J. (2014). $^{10}$Be exposure dating of river terraces at the southern mountain front of the Dzungarian Alatau (SE Kazakhstan) reveals rate of thrust faulting over the past ~400 ka. *Quaternary Research*, *81*(1), 168–178. https://doi.org/10.1016/j.yqres.2013.10.016

De Grave, J., Buslov, M. M., & Van den haute, P. (2007). Distant effects of India-Eurasia convergence and Mesozoic intracontinental deformation in Central Asia: Constraints from apatite fission-track thermochronology. *Journal of Asian Earth Sciences*, *29*(2), 188–204. https://doi.org/10.1016/j.jseaes.2006.03.001

Delvaux, D., Abdrakhmatov, K. E., Lemzin, I. N., & Strom, A. L. (2001). Landslide and surface breaks of the 1911 Ms 8.2 Kemin earthquake, Kyrgyzstan. *Landslides*, *42*(10), 1583–1592.

Dodds, N., Begenjev, G., Bezmenov, Y., Gruetzner, C., Mirzin, R., Rhodes, E., et al. (2022). A major Medieval earthquake on the main Köpetdag (Kopeh Dagh) Fault, Turkmenistan. *Bulletin-Seismological Society of America*, *112*, 2189–2215. https://doi.org/10.1785/0120210195

Dziewonski, A. M., Chou, T.-A., & Woodhouse, J. H. (1981). Determination of earthquake source parameters from waveform data for studies of global and regional seismicity. *Journal of Geophysical Research*, *86*(B4), 2825–2852. https://doi.org/10.1029/JB086iB04p02825

Ekström, G., Nettles, M., & Dziewonski, A. M. (2012). The global CMT project 2004–2010: Centroid-moment tensors for 13,017 earthquakes. *Physics of the Earth and Planetary Interiors*, *200–201*, 1–9. https://doi.org/10.1016/j.pepi.2012.04.002

Elliott, A. J., Oskin, M. E., Liu-zeng, J., & Shao, Y. X. (2015). Rupture termination at restraining bends: The last great earthquake on the Altyn Tagh Fault. *Geophysical Research Letters*, *42*, 2164–2170. https://doi.org/10.1002/2015GL063107

England, P., & Molnar, P. (1997). The field of crustal velocity in Asia calculated from Quaternary rates of slip on faults. *Geophysical Journal International*, *130*(3), 551–582. https://doi.org/10.1111/j.1365-246X.1997.tb01853.x

Fletcher, J. M., Oskin, M. E., & Teran, O. J. (2016). The role of a keystone fault in triggering the complex El Mayor-Cucapah earthquake rupture. *Nature Geoscience*, *9*(4), 303–307. https://doi.org/10.1038/ngeo2660

Ghose, S., Mellors, R. J., Korjenkov, A. M., Hamburger, M. W., Pavlis, T. L., Pavlis, G. L., et al. (1997). The MS = 7.3 1992 Suusamyr, Kyrgyzstan, earthquake in the Tien Shan: 2. Aftershock focal mechanisms and surface deformation. *Bulletin of the Seismological Society of America*, *87*(1), 23–38.

Grützner, C., Carson, E., Walker, R. T., Rhodes, E. J., Mukambayev, A., Mackenzie, D., et al. (2017a). Assessing the activity of faults in continental interiors: Palaeoseismic insights from SE Kazakhstan. *Earth and Planetary Science Letters*, *459*, 93–104. https://doi.org/10.1016/j.epsl.2016.11.025

Grützner, C., Walker, R. T., Abdrakhmatov, K. E., Mukambayev, A., Elliott, A. J., & Elliott, J. R. (2017b). Active tectonics around Almaty and along the Zailisky Alatau Rangefront. *Tectonics*, *36*, 2192–2226. https://doi.org/10.1002/2017TC004657

Haeussler, P. J., Schwartz, D. P., Dawson, T. E., Stenner, H. D., Lienkaemper, J. J., Sherrod, B., et al. (2004). Surface rupture and slip distribution of the Denali and Totschunda Faults in the 3 November 2002 M 7.9 Earthquake, Alaska. *Bulletin of the Seismological Society of America*, *94*(6B), S23–S52. https://doi.org/10.1785/0120040626

Hanks, T. C. (2000). The age of Scarplike landforms from diffusion-equation Analysis. In J. S. Noller, J. M. Sowers, & W. R. Lettis (Eds.), *Quaternary geochronology: Methods and applications* (Vol. 4, pp. 313–338). American Geophysical Union.

Hay, M. B. (1888). The earthquakes of May and June, 1887, in the Verny (Vernoe) District, Russian Turkestan, and their consequences. *Proceedings of the Royal Geographical Society and Monthly Record of Geography*, *10*(10), 638–646. https://doi.org/10.2307/1800851

Hendrix, M. S., Graham, S. A., Carroll, A. R., Sobel, E. R., McKnight, C. L., Schulein, B. J., & Wang, Z. (1992). Sedimentary record and climatic implications of recurrent deformation in the Tian Shan: Evidence from Mesozoic strata of the north Tarim, south Junggar, and Turpan basins, northwest China. *GSA Bulletin*, *104*(1), 53–79. https://doi.org/10.1130/0016-7606(1992)104<0053:sracio>2.3.co;2;2

Hollingsworth, J., Ye, L., & Avouac, J.-P. (2017). Dynamically triggered slip on a splay fault in the Mw 7.8, 2016 Kaikoura (New Zealand) earthquake. *Geophysical Research Letters*, *44*, 3517–3525. https://doi.org/10.1002/2016GL072228

Hu, Z. (2019). *Activity of the Jinghe section of the Bolokenu-Aqikekuduk Fault since the late Pleistocene (Master Thesis)*. Beijing, China: Institute of Geology, China Earthquake Administration.

Hu, Z., Yang, X., Yang, H., Huang, W., Wu, G., Miao, S., & Zhang, L. (2021). Slip rate and paleoseismology of the Bolokenu-Aqikekuduk (Dzhungarian) right-lateral strike-slip fault in the Northern Tian Shan, NW China. *Tectonics*, *40*, e2020TC006604. https://doi.org/10.1029/2020TC006604

Huntley, D. J., & Baril, M. R. (1997). The K content of the K-feldspars being measured in optical dating or in thermoluminescence dating. *Ancient Tl*, *15*(1), 11–13.

Jackson, J. A., McKenzie, D., & Priestley, K. (2021). Relations between earthquake distributions, geological history, tectonics and rheology on the continents. *Philosophical Transactions of the Royal Society A: Mathematical, Physical & Engineering Sciences*, *379*(2193), 20190412. https://doi.org/10.1098/rsta.2019.0412

Kalmeteva, Z. A., Mikolaichuk, A., Moldobekov, B. D., Meleshko, A. V., Jantaev, M. M. M., Zubovich, A. V., & Havenith, H. B. (2009). Atlas of earthquakes in Kyrgyzstan. In *CAIAG, Bishkek (Issue January)*.

Kanamori, H. (1977). The energy release in great earthquakes. *Journal of Geophysical Research*, *82*(20), 2981–2987. https://doi.org/10.1029/JB082i020p02981

Kanamori, H., & Anderson, D. L. (1975). Theoretical basis of some empirical relations in seismology. *Bulletin of the Seismological Society of America*, *65*(5), 1073–1095.

King, T. R., Quigley, M., & Clark, D. (2019). Surface-rupturing historical earthquakes in Australia and their environmental effects: New insights from re-analyses of observational data. *Geosciences*, *9*(10), 408. https://doi.org/10.3390/geosciences9100408

Klinger, Y., Etchebes, M., Tapponnier, P., & Narteau, C. (2011). Characteristic slip for five great earthquakes along the Fuyun fault in China. *Nature Geoscience*, *4*(6), 389–392. https://doi.org/10.1038/ngeo1158

Kondorskaya, N. V., & Shebalin, N. (1977). *New catalog of strong earthquakes in the USSR from ancient times through 1977*. Moscow: Academy of Sciences (English translation, updated through 1977, available as Report SE-31, World Data Center A for Solid Earth Geophysics, Boulder, CO).

Krüger, F., Kulikova, G., & Landgraf, A. (2017). Instrumental magnitude constraints for the 11 July 1889, Chilik earthquake. *Geological Society, London, Special Publications*, *432*(1), 41–72. https://doi.org/10.1144/SP432.8

Kulikova, G., & Krüger, F. (2015). Source process of the 1911 M8.0 Chon-Kemin earthquake: Investigation results by analogue seismic records. *Geophysical Journal International*, *201*(3), 1891–1911. https://doi.org/10.1093/gji/ggv091

Kurtz, R., Klinger, Y., Ferry, M., & Richter, C. F. (2018). Horizontal surface-slip distribution through several seismic cycles: The Eastern Bogd fault, Gobi-Altai, Mongolia. *Tectonophysics*, *734–735*(March), 167–182. https://doi.org/10.1016/j.tecto.2018.03.011



19449194, 2022, 10, Downloaded from https://agupubs.onlinelibrary.wiley.com/doi/10.1029/2022TC007300 by Test, Wiley Online Library on [10/01/2023]. See the Terms and Conditions (https://onlinelibrary.wiley.com/terms-and-conditions) on Wiley Online Library for rules of use; OA articles are governed by the applicable Creative Commons License

Lee, J.-C., Chu, H.-T., Angelier, J., Chan, Y.-C., Hu, J.-C., Lu, C.-Y., & Rau, R.-J. (2002). Geometry and structure of northern surface ruptures of the 1999 Mw=7.6 Chi-Chi Taiwan earthquake: Influence from inherited fold belt structures. *Journal of Structural Geology*, *24*(1), 173–192. https://doi.org/10.1016/S0191-8141(01)00056-6

Leonard, M. (2010). Earthquake fault scaling: Self-consistent relating of rupture length, width, average displacement, and moment release. *Bulletin of the Seismological Society of America*, *100*(5A), 1971–1988. https://doi.org/10.1785/0120090189

Li, Q., Liu, M., & Stein, S. (2009). Spatiotemporal complexity of continental intraplate seismicity: Insights from geodynamic modeling and implications for seismic hazard estimation. *Bulletin of the Seismological Society of America*, *99*(1), 52–60. https://doi.org/10.1785/0120080005

Liu, M., & Stein, S. (2016). Mid-continental earthquakes: Spatiotemporal occurrences, causes, and hazards. *Earth-Science Reviews*, *162*, 364–386. https://doi.org/10.1016/j.earscirev.2016.09.016

Lu, R., He, D., Xu, X., Wang, X., Tan, X., & Wu, X. (2018). Seismotectonics of the 2016 M 6.2 Hutubi Earthquake: Implications for the 1906 M 7.7 Manas earthquake in the Northern Tian Shan Belt, China. *Seismological Research Letters*, *89*(1), 13–21. https://doi.org/10.1785/0220170123

Ma, K. F., & Mori, J. (2000). Rupture process of the 1999 Chi-Chi, Taiwan Earthquake from direct observations and joint inversion of strong motion, GPS and teleseismic data. 2000 Western Pacific Geophysics Meeting.

Mackenzie, D., & Elliott, A. J. (2017). Untangling tectonic slip from the potentially misleading effects of landform geometry. *Geosphere*, *13*(4), 1310–1328. https://doi.org/10.1130/GES01386.1

Manighetti, I., Campillo, M., Bouley, S., & Cotton, F. (2007). Earthquake scaling, fault segmentation, and structural maturity. *Earth and Planetary Science Letters*, *253*(3–4), 429–438. https://doi.org/10.1016/j.epsl.2006.11.004

McCalpin, J. P., & Carver, G. A. (2009). Paleoseismology. *International Geophysics*, *95*, 315–419. https://doi.org/10.1016/s0074-6142(09)95005-7

Middleton, T., Walker, R. T., Parsons, B., Lei, Q., Zhou, Y., & Ren, Z. (2015). A major, intraplate, normal-faulting earthquake: The 1739 Yinchuan event in northern China. *Journal of Geophysical Research: Solid Earth*, *4*, 293–320. https://doi.org/10.1002/2015JB012355

Molnar, P., & Ghose, S. (2000). Seismic moments of major earthquakes and the rate of shortening across the Tien Shan. *Geophysical Research Letters*, *27*(16), 2377–2380. https://doi.org/10.1029/2000GL011637

Molnar, P., & Tapponnier, P. (1975). Cenozoic tectonics of Asia: Effects of a continental collision. *Science*, *30*(3), 213–219.

Mosca, I., Baptie, B., Sargeant, S., & Walker, R. T. (2019). Integrating outcomes from probabilistic and deterministic seismic hazard analysis in the Tien Shan. *Bulletin of the Seismological Society of America*, *109*(2), 688–715. https://doi.org/10.1785/0120180081

Mushketov, I. V. (1890). Le tremblement de terre de Verny, 28 Mai (9 Juin) 1887. *Memoires Du Comite Geologique*, *X*(1).

Mushketov, I. V., & Orlov, A. P. (1893). *Catalog of earthquakes of the Russian Empire (in Russian)*. St. Petersburg: Russian Geological Society.

Nash, D. B. (1980). Morphologic dating of degraded normal fault scarps. *The Journal of Geology*, *88*(3), 353–360. https://doi.org/10.1086/628513

Negishi, H., Mori, J., Sato, T., Singh, R., Kumar, S., & Hirata, N. (2002). Size and orientation of the fault plane for the 2001 Gujarat, India earthquake (Mw7.7) from aftershock observations: A high stress drop event. *Geophysical Research Letters*, *29*(20), 1949. https://doi.org/10.1029/2002GL015280

Ou, Q., Kulikova, G., Yu, J., Elliott, A. J., Parsons, B., & Walker, R. T. (2020). Magnitude of the 1920 Haiyuan Earthquake reestimated using seismological and geomorphological methods. *Journal of Geophysical Research: Solid Earth*, *125*, e2019JB019244. https://doi.org/10.1029/2019JB019244

Pang, L., Lu, H., Wu, D., Guan, X., Zhao, J., Zheng, X., & Li, Y. (2021). Late Pleistocene uniform rate of thrusting along the Fault's strike: A case study from the Northern Tian Shan Foreland. *Tectonics*, *40*, e2021TC006726. https://doi.org/10.1029/2021TC006726

Pantosti, D., Schwartz, D. P., & Valensise, G. (1993). Paleoseismology along the 1980 surface rupture of the Irpinia fault: Implications for earthquake recurrence in the southern Apennines, Italy. *Journal of Geophysical Research*, *98*(B4), 6561–6577. https://doi.org/10.1029/92JB02277

Pierce, I., Wesnousky, S. G., Owen, L. A., Bormann, J. M., Li, X., & Caffee, M. (2021). Accommodation of plate motion in an Incipient strike-slip system: The Central Walker Lane. *Tectonics*, *40*, e2019TC005612. https://doi.org/10.1029/2019TC005612

Pierce, K. L., & Colman, S. M. (1986). Effect of height and orientation (microclimate) on geomorphic degradation rates and processes, late-glacial terrace scarps in central Idaho. *The Geological Society of America Bulletin*, *97*(7), 869–885. https://doi.org/10.1130/0016-7606(1986)97<869:eohaom>2.0.co;2:EOHAOM>2.0.CO;2

Quigley, M., Jiménez, A., Duffy, B., & King, T. R. (2019). Physical and statistical behavior of multifault earthquakes: Darfield earthquake case study, New Zealand. *Journal of Geophysical Research: Solid Earth*, *124*, 4788–4810. https://doi.org/10.1029/2019JB017508

Quigley, M., Van Dissen, R., Litchfield, N., Villamor, P., Duffy, B., Barrell, D., et al. (2012). Surface rupture during the 2010 Mw 7.1 Darfield (Canterbury) earthquake: Implications for fault rupture dynamics and seismic-hazard analysis. *Geology*, *40*(1), 55–58. https://doi.org/10.1130/G32528.1

Rhodes, E. J. (2015). Dating sediments using potassium feldspar single-grain IRSL: Initial methodological considerations. *Quaternary International*, *362*, 14–22. https://doi.org/10.1016/j.quaint.2014.12.012

Rhodes, E. J., Fanning, P. C., & Holdaway, S. J. (2010). Developments in optically stimulated luminescence age control for geoarchaeological sediments and hearths in western New South Wales, Australia. *Quaternary Geochronology*, *5*(2), 348–352. https://doi.org/10.1016/j.quageo.2009.04.001

Rizza, M., Abdrakhmatov, K. E., Walker, R. T., Braucher, R., Guillou, V., Carr, A. S., et al. (2019). Rate of slip from multiple quaternary dating methods and paleoseismic investigations along the Talas-Fergana Fault: Tectonic implications for the Tien Shan range. *Tectonics*, *38*, 2477–2505. https://doi.org/10.1029/2018TC005188

Rizza, M., Richter, C. F., Prentice, C., Vassallo, R., Braucher, R., Larroque, C., et al. (2015). Earthquake geology of the Bulnay fault (Mongolia). *Bulletin of the Seismological Society of America*, *105*(1), 72–93. https://doi.org/10.1785/0120140119

Rodgers, D. W., & Little, T. A. (2006). World's largest coseismic strike-slip offset: The 1855 rupture of the Wairarapa Fault, New Zealand, and implications for displacement/length scaling of continental earthquakes. *Journal of Geophysical Research*, *111*, B12408. https://doi.org/10.1029/2005JB004065

Rogozhin, E. A., Shen, J., Chen, Q., & Shen, X. (2015). Paleoseismic ruptures in the potential seismic source of major earthquakes in the Dzhungar Tien Shan. *Seismic Instruments*, *51*(2), 99–110. https://doi.org/10.3103/s0747923915020073

Ross, Z. E., Idini, B., Jia, Z., Stephenson, O. L., Zhong, M., Wang, X., et al. (2019). Hierarchical interlocked orthogonal faulting in the 2019 Ridgecrest earthquake sequence. *Science*, *366*(6463), 346–351. https://doi.org/10.1126/science.aaz0109

Salditch, L., Stein, S., Neely, J., Spencer, B. D., Brooks, E. M., Agnon, A., & Liu, M. (2020). Earthquake supercycles and long-term fault memory. *Tectonophysics*, *774*, 228289. https://doi.org/10.1016/j.tecto.2019.228289

Satake, K., Fujii, Y., Harada, T., & Namegaya, Y. (2013). Time and space distribution of coseismic slip of the 2011 Tohoku earthquake as inferred from tsunami waveform data. *Bulletin of the Seismological Society of America*, *103*(2B), 1473–1492. https://doi.org/10.1785/0120120122

Schmidt, D. A., & Bürgmann, R. (2006). InSAR constraints on the source parameters of the 2001 Bhuj earthquake. *Geophysical Research Letters*, *33*, L02315. https://doi.org/10.1029/2005GL025109



19449194, 2022, 10, Downloaded from https://agupubs.onlinelibrary.wiley.com/doi/10.1029/2022TC007300 by Test, Wiley Online Library on [10/01/2023]. See the Terms and Conditions (https://onlinelibrary.wiley.com/terms-and-conditions) on Wiley Online Library for rules of use; OA articles are governed by the applicable Creative Commons License

Scholz, C. H. (1982). Scaling laws for large earthquakes: Consequences for physical models. *The Geographical Journal*, *48*(4), 348. https://doi.org/10.2307/1779766

Scholz, C. H. (1986). Scaling differences between large interplate and intraplate earthquakes. *Bulletin of the Seismological Society of America*, *76*(1), 65–70.

Seismological Bureau of Xinjiang. (1985). Compilation of seismic data in Xinjiang Uygur autonomous region (in Chinese) (pp. 38–44). Beijing, China: Seismological Press.

Selander, J., Oskin, M. E., Ormukov, C., & Abdrakhmatov, K. E. (2012). Inherited strike-slip faults as an origin for basement-cored uplifts: Example of the Kungey and Zailiskey ranges, northern Tian Shan. *Tectonics*, *31*, TC4026. https://doi.org/10.1029/2011TC003002

Shean, D. (2017). *High Mountain Asia 8-meter DEM mosaics derived from optical imagery, Version 1*. Boulder, CO: NASA National Snow and Ice Data Center Distributed Active Archive Center. https://doi.org/10.5067/KXOVQ9L172S2

Shen, J., Wang, Y., & Li, Y. (2011). Characteristics of the late Quaternary right-lateral strike-slip movement of Bolokenu-Aqikekuduk Fault in northern Tianshan Mountains, NW China. *Geoscience Frontiers*, *2*(4), 519–527. https://doi.org/10.1016/j.gsf.2011.05.004

Shimazaki, K., & Nakata, T. (1980). Time-predictable recurrence model for large earthquakes. *Geophysical Research Letters*, *7*(4), 279–282. https://doi.org/10.1029/GL007i004p00279

Sieh, K. (1978). Prehistoric large earthquakes produced by slip on the San Andreas fault at Pallett Creek, California. *Journal of Geophysical Research*, *83*(B8), 3907–3939. https://doi.org/10.1029/JB083iB08p03907

Sieh, K. (1996). The repetition of large-earthquake ruptures. *Proceedings of the National Academy of Sciences of the United States of America*, *93*(9), 3764–3771. https://doi.org/10.1073/pnas.93.9.3764

Sieh, K., Jones, L., Hauksson, E., Hudnut, K., Eberhart-Phillips, D., Heaton, T., et al. (1993). Near-field investigations of the Landers Earthquake Sequence, April to July 1992. *Science*, *260*(5105), 171–176. https://doi.org/10.1126/science.260.5105.171

Simpson, D. W., Hamburger, M. W., Pavlov, V. D., & Nersesov, I. L. (1981). Tectonics and seismicity of the Toktogul Reservoir Region, Kirgizia, USSR. *Journal of Geophysical Research*, *86*(B1), 345–358. https://doi.org/10.1029/JB086iB01p00345

Sloan, R. A., Jackson, J. A., McKenzie, D., & Priestley, K. (2011). Earthquake depth distributions in Central Asia, and their relations with lithosphere thickness, shortening and extension. *Geophysical Journal International*, *185*(1), 1–29. https://doi.org/10.1111/j.1365-246X.2010.04882.x

Spelz, R. M., Fletcher, J. M., Owen, L. A., & Caffee, M. (2008). Quaternary alluvial-fan development, climate and morphologic dating of fault scarps in Laguna Salada, Baja California, Mexico. *Geomorphology*, *102*(3–4), 578–594. https://doi.org/10.1016/j.geomorph.2008.06.001

Stahl, T. A., Cowgill, E., Boichenko, G., Vasey, D. A., & Godoladze, T. (2022). Recent surface rupturing earthquakes along the South Flank of the Greater Caucasus near Tbilisi, Georgia. *Bulletin of the Seismological Society of America*, *112*, 2170–2188. https://doi.org/10.1785/0120210267

Stein, S., Liu, M., Calais, E., & Li, Q. (2009). Mid-continent earthquakes as a complex system. *Seismological Research Letters*, *80*(4), 551–553. https://doi.org/10.1785/gssrl.80.4.551

Stewart, N., Gaudemer, Y., Manighetti, I., Serreau, L., Vincendeau, A., Dominguez, S., et al. (2018). "3D_Fault_Offsets," a Matlab code to automatically measure lateral and vertical fault offsets in topographic data: Application to San Andreas, Owens Valley, and Hope Faults. *Journal of Geophysical Research: Solid Earth*, *123*, 815–835. https://doi.org/10.1002/2017JB014863

Stockmeyer, J. M., Shaw, J. H., & Guan, S. (2014). Seismic hazards of multisegment thrust-fault ruptures: Insights from the 1906 Mw 7.4-8.2 Manas, China, Earthquake. *Seismological Research Letters*, *85*(4), 801–808. https://doi.org/10.1785/0220140026

Tapponnier, P., & Molnar, P. (1979). Active faulting and cenozoic tectonics of the Tien Shan, Mongolia, and Baykal Regions. *Journal of Geophysical Research*, *84*(B7), 3425–3459. https://doi.org/10.1029/JB084iB07p03425

Thingbaijam, K. K. S., Mai, P. M., & Goda, K. (2017). New empirical earthquake source-scaling laws. *Bulletin of the Seismological Society of America*, *107*(5), 2225–2246. https://doi.org/10.1785/0120170017

Thompson, S. C. (2001). *Active tectonics in the central Tien Shan, Kyrgyz Republic (Doctoral Dissertation)*. University of Washington.

Thompson, S. C., Weldon, R. J., Rubin, C. M., Abdrakhmatov, K. E., Molnar, P., & Berger, G. W. (2002). Late Quaternary slip rates across the central Tien Shan, Kyrgyzstan, Central Asia. *Journal of Geophysical Research*, *107*(B9), 2203. https://doi.org/10.1029/2001JB000596

Tsai, C.-H., Walker, R. T., Daout, S., Abdrakhmatov, K., Mukambayev, A., Grützner, C., et al. (2021). *Great earthquakes in the Dzhungarian region interpreted from palaeo- and historical sources: Implications for intraplate earthquake occurrence and scaling*. AGU Fall Meeting 2021.

Vilgelmzon, P. M. (1947). *Kemin-chu earthquake of July 21, 1938* (Vol. 40). Academy of Sciences of the Kazakh, Almaty SSR.

Voytovich, V. S. (1965). Development of Dzhungar deep fault. *International Geology Review*, *7*(5), 874–883. https://doi.org/10.1080/00206816509474154

Voytovich, V. S. (1969). Nature of the Dzungarian deep fault (in Russian). *Transmission of Geology Institute, Academy of Sciences of the USSR*, *183*, 189.

Walker, R. T., Bezmenov, Y., Begenjev, G., Carolin, S., Dodds, N., Grützner, C., et al. (2021). Slip-rate on the Main Köpetdag (Kopeh Dagh) strike-slip fault, Turkmenistan, and the active tectonics of the South Caspian. *Tectonics*, *40*, e2021TC006846. https://doi.org/10.1029/2021TC006846

Walker, R. T., Wegmann, K. W., Bayasgalan, A., Carson, R. J., Elliott, J. R., Fox, M., et al. (2017). The Egiin Davaa prehistoric rupture, central Mongolia: A large magnitude normal faulting earthquake on a reactivated fault with little cumulative slip located in a slowly deforming intraplate setting. *Geological Society Special Publication*, *432*(1), 187–212. https://doi.org/10.1144/SP432.4

Wallace, R. (1970). Earthquake recurrence intervals on the San Andreas fault. *Bulletin of the Geological Society of America*, *81*(10), 2875–2889. https://doi.org/10.1130/0016-7606(1970)81[2875:eriots]2.0.co;2:ERIOTS]2.0.CO;2

Wallace, R. (1977). Profiles and ages of young fault scarps, north-central Nevada. *GSA Bulletin*, *88*(9), 1267–1281. https://doi.org/10.1130/0016-7606(1977)88<1267:paaoyf>2.0.co;2.CO;2

Wang, C. Y., Yang, Z. E., Luo, H., & Mooney, W. D. (2004). Crustal structure of the northern margin of the eastern Tien Shan, China, and its tectonic implications for the 1906 M∼7.7 Manas earthquake. *Earth and Planetary Science Letters*, *223*(1–2), 187–202. https://doi.org/10.1016/j.epsl.2004.04.015

Wells, D. L., & Coppersmith, K. J. (1994). New empirical relationships among magnitude, rupture length, rupture width, rupture area, and surface displacement. *Bulletin of the Seismological Society of America*, *84*(4), 974–1002.

Wesnousky, S. G. (2008). Displacement and geometrical characteristics of earthquake surface ruptures: Issues and implications for seismic-hazard analysis and the process of earthquake rupture. *Bulletin of the Seismological Society of America*, *98*(4), 1609–1632. https://doi.org/10.1785/0120070111

Westoby, M. J., Brasington, J., Glasser, N. F., Hambrey, M. J., & Reynolds, J. M. (2012). "Structure-from-Motion" photogrammetry: A low-cost, effective tool for geoscience applications. *Geomorphology*, *179*, 300–314. https://doi.org/10.1016/j.geomorph.2012.08.021

Windley, B. F., Alexeiev, D., Xiao, W., Kröner, A., & Badarch, G. (2007). Tectonic models for accretion of the Central Asian Orogenic Belt. *Journal of the Geological Society*, *164*(1), 31–47. https://doi.org/10.1144/0016-76492006-022



19449194, 2022, 10, Downloaded from https://agupubs.onlinelibrary.wiley.com/doi/10.1029/2022TC007300 by Test, Wiley Online Library on [10/01/2023]. See the Terms and Conditions (https://onlinelibrary.wiley.com/terms-and-conditions) on Wiley Online Library for rules of use; OA articles are governed by the applicable Creative Commons License

Windley, B. F., Allen, M. B., Zhang, C., Zhao, Z.-Y., & Wang, G.-R. (1990). Paleozoic accretion and Cenozoic redeformation of the Chinese Tien Shan range, Central Asia. *Geology*, *18*(2), 128–131. https://doi.org/10.1130/0091-7613(1990)018<0128:paacro>2.3.co;2.CO;2

Wu, C., Ren, G., Yu, J., Zheng, W., Li, X., Liu, J., et al. (2020). Oblique right-lateral faulting along the northern margin of the Ili Basin in the Northern Tian Shan, Northwest China. *Tectonics*, *39*, e2020TC006061. https://doi.org/10.1029/2020TC006061

Wu, C., Wang, W., Zheng, W., Zhang, P., & Yu, Z. (2021). Opposite sense of strike-slip faulting and crustal rotation accommodating left-lateral shear between the Tianshan Mountains and Kazakh Platform. *Geophysical Research Letters*, *48*, e2021GL096442. https://doi.org/10.1029/2021GL096442

Xu, W., Feng, G., Meng, L., Zhang, A., Ampuero, J. P., Bürgmann, R., & Fang, L. (2018). Transpressional Rupture Cascade of the 2016 Mw 7.8 Kaikoura Earthquake, New Zealand. *Journal of Geophysical Research: Solid Earth*, *123*, 2396–2409. https://doi.org/10.1002/2017JB015168

Yang, H., Quigley, M., & King, T. R. (2021). Surface slip distributions and geometric complexity of intraplate reverse-faulting earthquakes. *Bulletin of the Geological Society of America*, *133*(9–10), 1909–1929. https://doi.org/10.1130/B35809.1

Yang, X., & Shen, J. (2000). Late quaternary activity of Jinghe-Alashankou section of the Boluokenu Fault, interior Tianshan. *Seismology and Geology*, *22*(3), 305–315.

Yang, Z., Guo, H.-Z., Ding, D.-X., & Xu, D.-Z. (1988). Finding of Tekes-Zhaosu Earthquake Faults in Xinjiang and some discussion. *Seismology and Geology*, *10*(3), 6.

Yin, G., Jiang, J. X., & Pei, H. D. (2006). The fault and the maximal displacement of Nilike earthquake in 1812. *Inland Earthquake*, *20*(4).

Zhang, P., Deng, Q., Xu, X., Peng, S., Yang, X., Feng, X., et al. (1994). Blind thrust, folding earthquake, and the 1906 Manas earthquake, Xinjiang (in Chinese). *Seismology and Geology*, *16*(3), 193–204.

Zhang, P., Min, W., Deng, Q., & Mao, F. (2005). Paleoearthquake rupture behavior and recurrence of great earthquakes along the Haiyuan fault, northwestern China. *Science in China-Series D: Earth Sciences*, *48*(3), 364–375. https://doi.org/10.1360/02yd0464

Zhou, Y., Parsons, B., Elliott, J. R., Barisin, I., & Walker, R. T. (2015). Assessing the ability of Pleiades stereo imagery to determine height changes in earthquakes: A case study for the El Mayor-Cucapah epicentral area. *Journal of Geophysical Research: Solid Earth*, *120*, 8793–8808. https://doi.org/10.1002/2015JB012358

Zielke, O., & Arrowsmith, J. R. (2012). LaDiCaoz and LiDARimager-MATLAB GUIs for LiDAR data handling and lateral displacement measurement. *Geosphere*, 8(1), 206–221. https://doi.org/10.1130/GES00686.1

Zielke, O., Arrowsmith, J. R., Ludwig, L. G., & Akciz, S. O. (2010). Slip in the 1857 and earlier large earthquakes along the Carrizo Plain, San Andreas Fault. *Science*, *327*(February), 1119–1123. https://doi.org/10.1126/science.1182781

Zinke, R., Dolan, J. F., Rhodes, E. J., Van Dissen, R., & McGuire, C. P. (2017). Highly variable latest Pleistocene-Holocene Incremental slip rates on the Awatere Fault at Saxton River, South Island, New Zealand, revealed by Lidar mapping and luminescence dating. *Geophysical Research Letters*, *44*, 11301–11310. https://doi.org/10.1002/2017GL075048

Zubovich, A. V., Wang, X. Q., Scherba, Y. G., Schelochkov, G. G., Reilinger, R. E., Reigber, C., et al. (2010). GPS velocity field for the Tien Shan and surrounding regions. *Tectonics*, *29*, TC6014. https://doi.org/10.1029/2010TC002772



19449194, 2022, 10, Downloaded from https://agupubs.onlinelibrary.wiley.com/doi/10.1029/2022TC007300 by Test, Wiley Online Library on [10/01/2023]. See the Terms and Conditions (https://onlinelibrary.wiley.com/terms-and-conditions) on Wiley Online Library for rules of use; OA articles are governed by the applicable Creative Commons License